Probabilistic Tsunami Hazard Assessment (PTHA) for Crescent City, CA

Final Report on Phase I

January 31, 2013

Frank I. González, Randall J. LeVeque, and Loyce M. Adams
University of Washington

Photo Source: http://tripsintohistory.com/wave-propagation-content/uploads/2012/03/800px-Crescent_City_California_harbor_aerial_viewUSArmyCorpofEngineeers1.jpg

Pilot Study funded by BakerAECOM

Contents

1 Executive Summary

This demonstration Probabilistic Tsunami Hazard Assessment (PTHA) study of Crescent City, California was funded by BakerAECOM and motivated by FEMA's desire to explore methods to improve products of the FEMA Risk Mapping, Assessment, and Planning (Risk MAP) Program. Here we briefly summarize the goals, primary results, conclusions, and recommendations of this study.

1.1 Goals

Initially, the overall goal was to

- Apply the numerical model, sources, and probabilistic methodology of the Seaside, Oregon PTHA study by González et. al. [12], to produce the following deliverables:
  - Maps of maximum wave height with 1% and 0.2% annual probabilities of exceedance
  - Maps of maximum flood depth with 1% and 0.2% annual probabilities of exceedance
  - Digital files of the map data
  - A final report

Once the study began, a number of issues arose that led us to add additional goals:

- Include Japan tsunamigenic seismic sources (*because the 2011 Tohoku event inflicted heavy damage on Crescent City and the West Coast – see Section 6.2 and Section 7.5*).
- Improve Cascadia Subduction Zone source specification (*because of advances in methods to generate stochastic seismic slip realizations, and because the Bandon, Oregon study by Witter, et. al. [40] clearly demonstrated the need for additional seismic scenarios – see Section 7.2 and Section 10.2*).
- Improve the method to estimate tidal uncertainty (*because Mofjeld et. al. [26] assumed tsunami waveforms significantly different than those measured and modeled at Crescent City and we had the capability with GeoClaw to make multiple runs of each potential tsunami at different tidal levels – see Section 8*).
- Explore non-regulatory products with potential value to improve or supplement current regulatory products (*because FEMA expressed a strong interest in such an effort – see Section 9.2*).
- Adopt the GeoClaw tsunami model and implement GeoClaw-compatible tools for post-processing analyses and visualization (*because efficient and user-friendly features of GeoClaw greatly facilitated addressing these additional goals*).

1.2 Primary Results, Conclusions, and Recommendations

The primary results, that is, the 100- and 500-year tsunami maps, are presented and discussed in Section 3 and Appendix C. These maps were generated by a significantly improved methodology than that of the Seaside study; the improvements include a more complete set of seismic sources (Table 1), and a more accurate method for estimating tidal uncertainty (Section 8). As expected, the inland extent and magnitude of the flooding for the 500-year tsunami far exceed that of the 100-year event; these products can now be compared with standard FEMA Flood Insurance Rate Maps (FIRMs) to determine whether these flooding levels exceed estimates of other coastal flooding hazards, such as storm surge. A final deliverable, digital data files of the map data, have been provided to BakerAECOM, and a description of these files is given in Appendix D.

The primary conclusion we have reached in the course of this study is that the maps must be used with caution because (a) there are significant uncertainties in the specifiation of CSZ seismic sources (Section 4 and Section 7.6) and (b) the standard 100- and 500-year maps are highly sensitive to these geophysical uncertainties and, in certain circumstances could even be misleading. Section 9.2 discusses this sensitivity in the context of a non-regulatory product that provides valuable additional insight by presenting the same probabilistic information in a different format that we call a p-contour map.

Finally, we recommend (a) that FEMA give serious consideration to the adoption of the p-contour map as a product that supplements and aids in the practical interpretation of the same probabilistic information displayed in the standard 100- and 500-year tsunami maps, and that (b) future PTHA studies should include close collaboration with a geoscientist expert in earthquake parameterization.

2 Introduction

This report documents the results of a pilot study supported by BakerAECOM to conduct a Probabilistic Tsunami Hazard Assessment (PTHA) of Crescent City, California for tsunamis generated by local and distant earthquakes. The project is part of a coastal modeling/mapping effort funded by the Federal Emergency Management Agency (FEMA) Region IX office as part of the new California Coastal Analysis and Mapping Project (CCAMP). In turn, CCAMP is being conducted under the nationwide FEMA Risk Mapping, Assessment, and Planning (Risk MAP) Program, which focuses on providing communities with flood information and tools to enhance their mitigation plans and better protect their citizens.

This report on Phase I of the project concerns only depth of inundation. Phase II is now in progress, in which similar analysis will be applied to tsunami currents and momentum flux.

2.1 Acknowledgements

Knut Waagan participated in many discussions on stochastic approaches and the possible development of new methodologies, with funding and mentoring provided by Guang Lin at the Pacific Northwest National Laboratory in Richland, WA. Many others have contributed ideas and insights that have guided the new approaches we suggest in this report, and/or provided guidance on aspects of the seismic modeling that is critical input to the tsunami modeling. In particular we want to acknowledge contributions of Brian Atwater, Art Frankel, Eric Geist, Finn Løvholt, Martin Mai, Geir Pedersen, Jonathan Varkovitzky, Tim Walsh, and Kelin Wang.

The GeoClaw software was developed in collaboration with David George and Marsha Berger, with recent contributions by Kyle Mandli and others. This software builds on the Clawpack software that many others have also contributed to.

2.2 Goals

The goals of this pilot project on probabilistic modeling are to:

- Develop best possible estimates of hazard maps for Crescent City based on the current state of scientific knowledge.

- In particular, produce "100-year" and "500-year" inundation maps, that illustrate the portion of Crescent City that is expected to flood with annual probability 0.01 and 0.002, respectively. For the inundated region, show contours of the maximum depth of flooding expected with these probabilities. See Section 3 for some examples of these "regulatory products."

- Develop new approaches to efficiently generating probabilistic maps related to tsunami hazards, including suggestions for new ways of viewing and interpreting the data.

2.3 Limitations

We have identified many sources of uncertainty in the course of this work that have been impossible to properly quantify, even probabilistically. These are discussed further in Section 4 and in the context of our results in later sections. We want to stress that all probabilistic maps generated as part of this study are themselves uncertain, and are based on assumptions about the probability distributions of possible earthquake sources that are often not well defined. They are our best estimates based on what we have been able to identify as the best available science. For more information on some of the sources of uncertainty, see Section 4 and Section 10.

It is also important to keep in mind that rare events do sometimes happen, and so even if the probabilistic maps were exactly correct, it could still happen that a region where the annual probability of inundation is extremely low could be flooded tomorrow if the corresponding event occurs.

2.4 Scientific approach

This study builds on and extends the PTHA work conducted at Seaside, Oregon, by González, et al. [12]. The methodology for this Crescent City PTHA is similar to that of the Seaside study, but includes the following improvements:

- Use of the GeoClaw software for each deterministic tsunami model. This code offers more flexibility (e.g. running at different tidal stages) than the MOST code used in the Seaside study. It also uses adaptive mesh refinement to improve the efficiency of individual runs. This software and validation studies that have been performed are described more in Section 5.
- New methods to estimate tidal uncertainty; see Section 8.
- The addition of a far-field source in Japan, based on information updated since the 3 March 2011 Tohoku tsunami (Japan Earthquake Research Committee, 2011); see Section 7.5.
- Generation of sample non-regulatory products that may prove useful when interpreting probabilistic results, in particular contour maps of probability of exceedance for different exceedance levels; see Section 9.2.

The first step in the PTHA analysis is to specify a suite of seismic sources, including estimates of their mean inter-event time T_M and a Poisson rate $\mu = 1/T_M$. Then the GeoClaw tsunami model is used to simulate generation, propagation and inundation corresponding to each seismic source, and a database is created of hazard indices, such as maximum flow depth and current velocity, on a fine resolution bathymetric/topographic grid of the Crescent City area. Actually three GeoClaw simulations are performed for each source, with three different static background water levels, in order to incorporate tidal uncertainty as described in Section 8. The database is then subjected to post-processing that creates a tsunami hazard curve at each position (x, y) of the Crescent City inundation grid. Each hazard curve provides probability of exceedance estimates for specific hazard index values that are then contoured and displayed in graphical form. Each of these steps is discussed in more detail below.

Figures 1 and 2 show Google Earth images of Crescent City at two scales. For this study the full region shown in Figure 1 has been studied, though many plots show only the downtown and harbor region seen in Figure 2 since many events do not inundate beyond this region.

Figure 2 also shows 6 synthetic gauge locations that are referred to in some later figures.

In each GeoClaw run, adaptive mesh refinement is used so that a range of different grid resolutions are used in different regions (as discussed more in Section 5), but in all cases the region shown in Figure 1 is refined to a resolution of 2/3 arcsecond on the finest computational grid. Periodically during the computation (roughly every 30 seconds), results from this grid are interpolated to a finer 1/3 arcsecond grid that covers the region of Figure 1 in order to monitor the maximum flow depth observed over the full computation at each point on the grid. The result of each run is a record of the maximum flow depth values at each point on a 865×541 grid (467965 grid points) covering the region of Figure 1, between longitude 235.77 and 235.85 degrees East, and between latitudes 41.735 and 41.785 degrees North. We use east longitude coordinates since the full computational domain often extended west of longitude 0, and we also wanted to use positive coordinates increasing from west to east.

2.5 Bathymetry and topography data

The bathymetric and topographic Digital Elevation Models (DEMs) used are the ETOPO1 global and Crescent City region grids, available online at the NOAA/NGDC website

http://www.ngdc.noaa.gov/dem/squareCellGrid/search.

A detailed description of the development of each, including the underlying bathy/topo source data and quality are provided in [2] and [13].

ETOPO1 global bathymetry with a resolution of 1 arcminute (approximately 2 km) was used over the ocean. This uses horizontal datum WGS84 and vertical datum MSL. For some farfield runs subsampled data at 4 arcminute resolution was used, consistent with the finest level grids used over most of the ocean. These datasets were obtained from

http://www.ngdc.noaa.gov/mgg/gdas/gd_designagrid.html.

For the region around Crescent City, 1/3 arcsecond (approximately 7.5 m by 10m resolution) bathymetry was used, obtained from

http://www.ngdc.noaa.gov/dem/squareCellGrid/download/693.

This uses horizontal datum WGS84 and vertical datum MHW. This was used for longitude 235.7655 to 235.84 and latitude 41.71643 to 41.7695.

Subsampled 1 arcsecond (approximately 22.5 m by 30 m) bathymetry was used for a larger region around Crescent City, from longitude 235 to 236 and latitude 41.42 to 42.1.

Onshore topography is bare earth, with no structures. The onshore topography in the Crescent City region is referenced to MHW, so $B = 0$ in contour plots corresponds to MHW,

Figure 1: Google Earth view of Crescent City. This is the region used for the study and maximum inundation for each each run is recorded at every point on a 1/3 arcsecond resolution grid covering this region.

which is roughly 0.77 m above MSL.

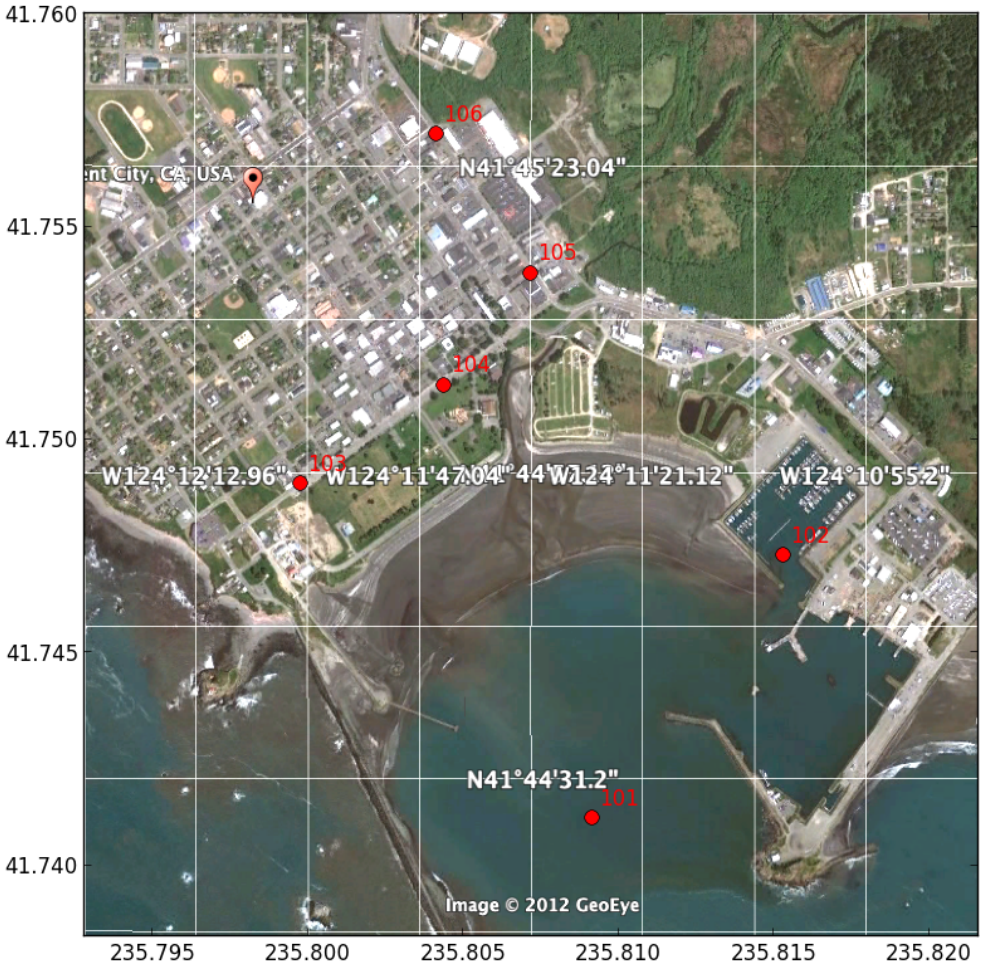

Figure 2: Zoom view of the harbor and downtown region. Gauges 101 through 106 in the computational results present below are indicated in this figure.

2.6 Notation and terminology

The following notation and terminology is used throughout this report.

- All depths and elevations are report in meters, since this is the convention for all datasets used.
- h refers to the water depth above topography or bathymetry. It is one of the primary variables of the shallow water equations.
- B refers to topography or bathymetry as specified by the topography datasets, and is relative to MHW since that is the vertical datum of the fine scale Crescent City bathymetry. Some CSZ events cause a change in the bathymetry in the Crescent City region (uplift or more typically subsidence). The plots are all presented relative to the pre-earthquake bathymetry.
- $\eta = B + h$ is the surface elevation relative to MHW.
- ζ will be used to denote the maximum observed value over the full time period of a tsunami of either h or $B + h$:

$$\zeta = \begin{cases} h, & \text{the flow depth, in regions where } B > 0 \text{ (onshore)}, \\ B + h, & \text{the sea surface elevation, in regions where } B < 0. \end{cases} \tag{1}$$

  Inundation and hazard maps generally show ζ. The sea surface elevation is relative to MHW.
- ξ denotes the tide stage, relative to MSL. With GeoClaw we can run the code with sealevel set to different values and this is used in the way we handle tidal uncertainty.
- Tsunami sources we used will generally be denoted in the form AASZe03, for example, which refers to event number 3 on the Alaska Aleutian Subduction Zone. Many events, such as AASZe03, have only one *realization* (model for how slip is distributed on the fault plane, and/or the resulting seafloor deformation). Some events, e.g. a CSZ Mw 9.1 event, have multiple possible realizations. For the CSZ event in this study, we use the 15 Bandon sources, see Witter, et.al. [40], as 15 realizations of one CSZ event, and refer to them as CSZBe01r01 – CSZBe01r15.

  In the probabilistic modeling we typically assign a recurrence time to the event and then a conditional probability to each realization of the event. If there is only one realization of the event, its conditional probability is 1.

2.6.1 Probabilities, rates, and recurrence times

By *probability of an event* we generally mean *annual probability of occurrence*. Specific earthquake events are often assumed to be governed by a Poisson process with some *mean recurrence time* T_M, in which case the annual probability of occurrence is $p = 1 - e^{-\nu}$ where the *rate* is $\nu = 1/T_M$. If ν is small then $p \approx \nu$ with an error that is $O(\nu^2)$. For example, if $T_M = 250$ then $\nu = 0.004$ and $p = 0.003992$. For larger T_M there is even less error. Since T_M is not accurately known, it is generally fine to assume $p = 1/T_M$.

When calculating the probability that one of several possible events might happen, some care is required. If two independent events are considered with annual probabilities p_1 and p_2 then the annual probability of at least one of them occurring is

$$p_{12} = 1 - (1 - p_1)(1 - p_2) = p_1 + p_2 - p_1 p_2.$$

If both probabilities are very small then $p_{12} \approx p_1 + p_2$ but for larger probabilities the more accurate expression must be used. Similarly, if we are interested in the probability of any one of N independent events occurring, the probability is

$$p_{1\ldots N} = 1 - (1 - p_1)(1 - p_2)\cdots(1 - p_N) \approx p_1 + p_2 + \cdots + p_N$$

Again simply adding the probabilities is valid only if the result is much less than one, but otherwise not.

Note that when expressed in terms of Poisson rates, it is valid to add the rates: if $p_i = 1 - e^{-\nu_i}$ then $p_{1\ldots N}$ has rate $\nu_1 + \nu_2 + \cdots + \nu_N$ since

$$p_{1\ldots N} = 1 - e^{-\nu_1} e^{-\nu_2} \cdots e^{-\nu_N} = 1 - e^{-(\nu_1 + \cdots + \nu_N)}.$$

3 Probabilistic results

The primary products of this study are the "100 year" and "500 year" flood maps shown below. These were computed as described in the remainder of this report, using all the earthquake sources of Section 7 and taking into account tidal uncertainty using the "pattern method" developed in Section 8.3.

3.1 The 100 year Flood: ζ-contours for $p = 0.01$

Figure 3 shows contours of ζ corresponding to $p = 0.01$. Recall from Section 2.6 that ζ is the maximum depth of fluid at on-shore points that are inundated, and is the maximum elevation above MHW for points offshore.

Each point in the region of a given color has an annual probability of 0.01 of inundation above the corresponding ζ value. These are determined by examining the hazard curve of each point and determining what value ζ corresponds to $p = 0.01$. The outer limits of the area colored thus show the limits of the "100-year flood".

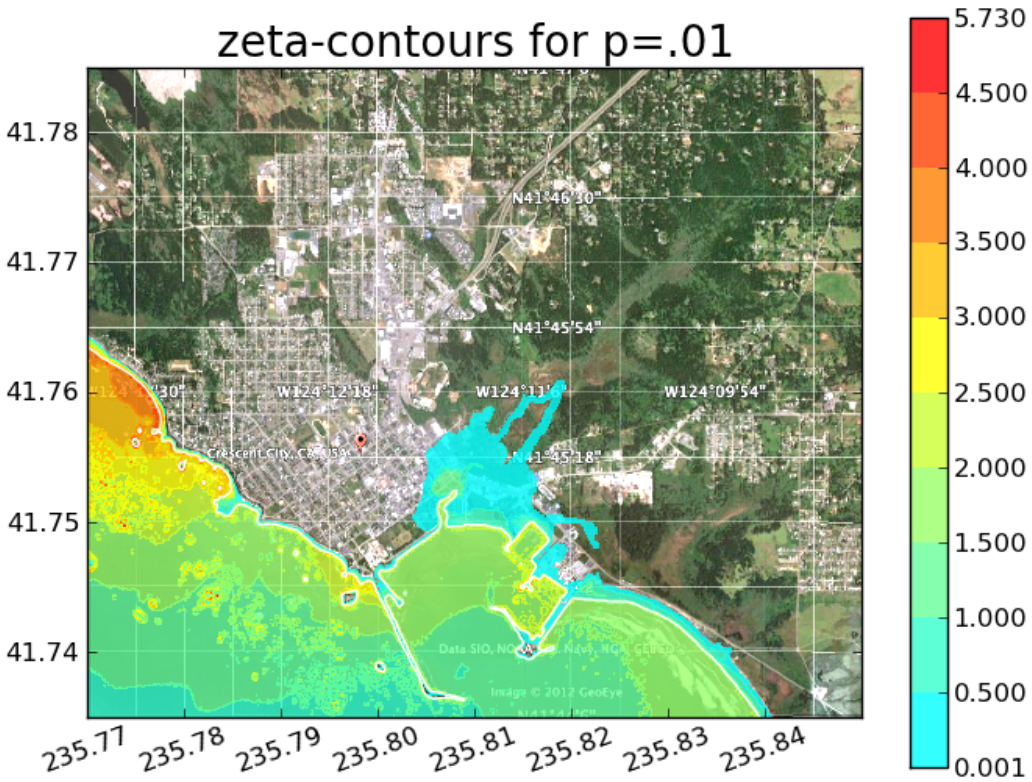

Figure 3: ζ-contours for p=.01. This product was created using all the study sources in Table 1. This includes the 15 Bandon study sources for CSZ with recurrence time $T_M = 332$ years and a representative Japan source with recurrence time $T_M = 103$ years. Note that ζ is the flow depth onshore and the height above MHW offshore, measured in meters.

3.2 The 500 year Flood: ζ-contours for $p = 0.002$

Similarly, Figure 4 shows contours of ζ corresponding to $p = 0.002$. Each point in the region of a given color has an annual probability of 0.002 of inundation above the corresponding ζ value. The outer limits of the area colored thus show the limits of the "500-year flood".

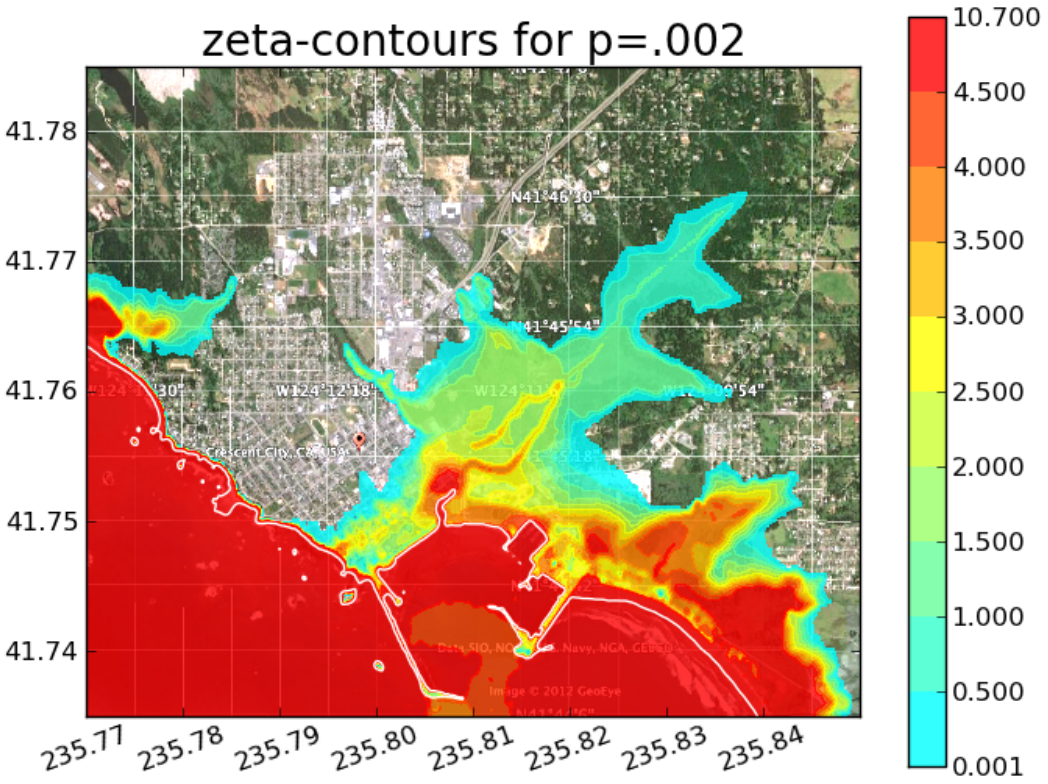

Figure 4: ζ-contours for p=.002. This product was created using all the study sources in Table 1. This includes the 15 Bandon study sources for CSZ with recurrence time $T_M = 332$ years and a representative Japan source with recurrence time $T_M = 103$ years. Note that ζ is the flow depth onshore and the height above MHW offshore, measured in meters.

These maps are the "regulatory products" specified as the desired results of this probabilistic study. We believe, however, that only looking at such maps may be misleading — the inundated region can be very sensitive to the probability levels chosen for display, or to the parameters used in the modeling, such as the recurrence time of one event. In Section 9.2 we show an example of this. We believe that it is possible to present the results of a probabilistic study in ways to convey additional information, and offer some suggestions in Section 9.2.

3.3 Hazard curves

The maps shown above and other probabilistic products described later are based on *hazard curves* that are constructed from the results of all individual GeoClaw runs over all the tsunami sources considered. Figure 5 shows typical hazard curves at four (x, y) points corresponding to the locations of Gauges 101, 103, 104, and 105 in Figure 2. The horizontal axis shows ζ as defined in Section 2.6, so it is the surface elevation above MHW at Gauge 101 and the flow depth at the other three locations. The vertical axis is *probability of exceedance*. At each ζ the corresponding $p(\zeta)$ approximates the annual probability of exceeding this value, at the particular (x, y) point.

These plots are generated as described in the following sections, and include tidal uncertainty as well as the probabilities of different earthquake events.

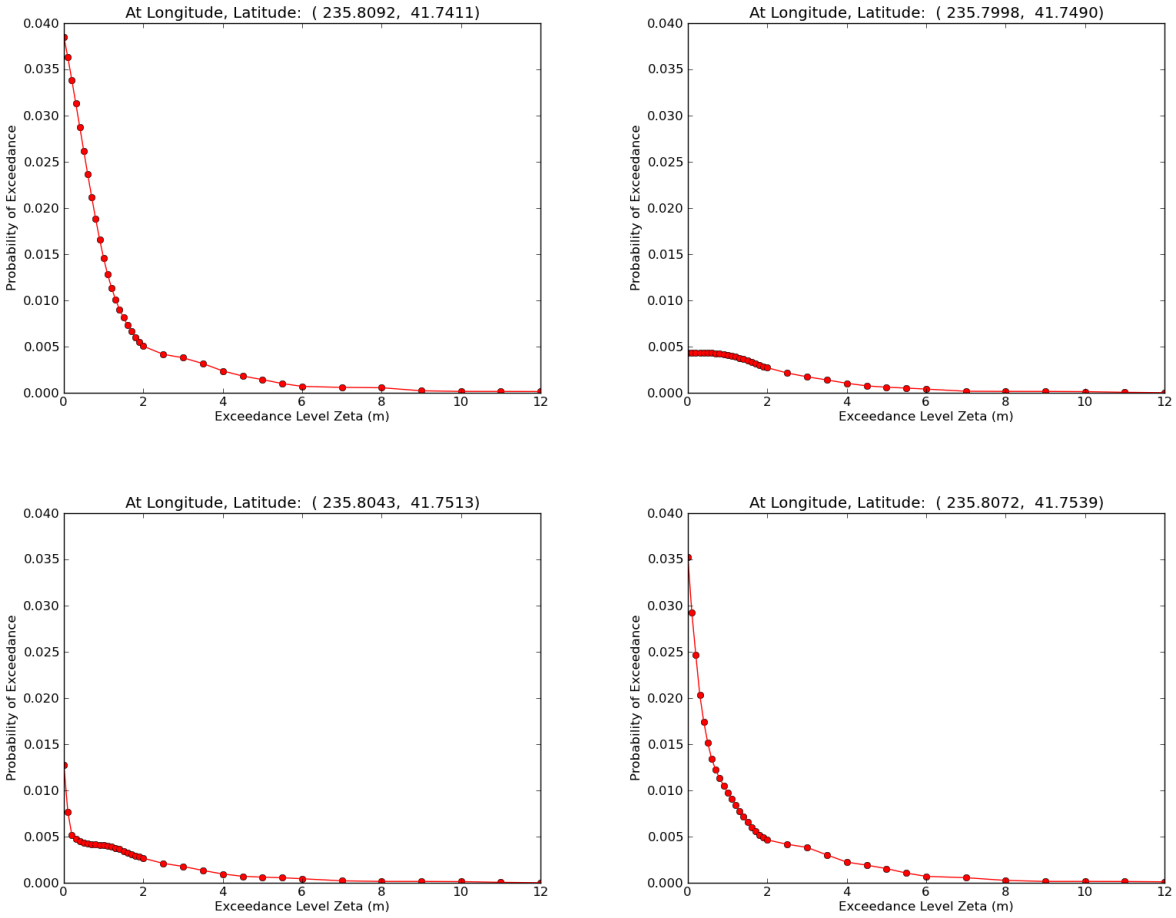

Figure 5: Sample hazard curves at four locations, Top: Gauges 101, 103, Bottom: Gauges 104, and 105 from Figure 2. Note that Gauge 101 is in the harbor, so ζ refers to the elevation above MHW. The other gauges are onshore and ζ refers to flow depth.

4 Sources of uncertainty

There are many sources of uncertainty that must feed into any probabilistic model of tsunami hazards. It is useful to distinguish between *epistemic* and *aleatoric* uncertainties, although it is not always possible to neatly divide all sources of uncertainty into one of these categories.

Aleatoric uncertainty refers to uncertainty due to the inherent randomness of the processes generating tsunamis. We can never know exactly when or where the next major earthquake will occur or how large it will be, let alone the details of the slip pattern on the fault that can affect the resulting inundation patterns. However, if we assume that we know suitable probability distributions (e.g. that one of a finite number of characteristic earthquakes might occur, and that they occur according to a Poisson process with known recurrence time), then we can use these probability distributions for the inputs in order to generate probability distributions of inundation at points in a community. There are challenges to doing this accurately and efficiently, but the desired output is a well defined probability distribution.

Epistemic uncertainty refers to uncertainty due to lack of knowledge of the underlying processes, which means we do not know the correct probability distributions for the inputs (and hence can't hope to produce the correct probability distribution for the output). For example, in general it is not known what the correct probability distribution is for how the slip might be distributed over the fault geometry. The fault geometry itself may not be well known. The time series of events is not simply a Poisson process and it is not even known what the correct mean recurrence time is in general for any particular event.

One can make a guess at what the right probability distribution is, or consider several possible probability distributions with some weighting. Doing the latter appears to reduce the epistemic uncertainty to another form of aleatoric uncertainty and may be useful in practice, but the philosophical difference is that epistemic uncertainty could in principle be eliminated if we had more information about the system. There is some correct probability distribution of possible events and if we could observe earthquakes for millions of years (and if the geophysical processes were time invariant) it might be possible to estimate the parameters describing this distribution arbitrarily well. On the other hand even if we knew the probability distribution exactly we would not have eliminated the aleatoric uncertainty described by this distribution — we still would not know which sample from this distribution the next earthquake will be or when it will occur.

Sources of uncertainty in PTHA include the following:

- Earthquake sources: This is a major source of uncertainty, and as discussed above there are large epistemic uncertainties in choosing the correct probability distribution of possible events. This is discussed in more detail in the coming sections.

- Tide stage: For a given earthquake and resulting tsunami, the extent and depth of inundation in Crescent City can vary greatly depending on whether the waves arrive at high tide or low tide. Since the earthquake might occur at any time in the tidal cycle with equal probability, this is a form of aleatoric uncertainty. There is little epistemic uncertainty since the probability that the tide will be greater than a given level at a

random time can be estimated very well by past tidal records and/or from the harmonic constituents that describe the expected future tides. There are still challenges in determining the best approach to incorporating this aleatoric uncertainty into the PTHA that are discussed further in Section 8. This is particularly interesting for earthquake sources where the resulting tsunamis consists of several large waves that hit Crescent City many hours apart, and for which the tide may change significantly in between.

- Sea level rise: In this report we have used topography and bathymetry data relevant for current sea level. If the resulting hazard maps are to be used for many years to come, perhaps the expected rise in sea level over the time horizon of interest should also be taken into account.

- Quality of bathymetry and topography data. The ocean bathymetry used comes from the ETOPO1 data set, which provides 1 arcminute resolution (about 2 km) over the entire Pacific Ocean. This is thought to be sufficiently accurate for our needs. Near Crescent City, 1 arcsecond and 1/3 arcsecond data is used as described in Section 2.5. This has sufficient spatial resolution, but there is some uncertainty regarding whether the vertical elevation data is adequate for detailed modeling in Crescent City. In particular, the data used gives the topography of "bare earth", without buildings or other structures. In reality inundation of the city center would entail water flowing through the streets and around many buildings. This will surely change the inundation patterns. To some extent this uncertainty can be investigated by running the simulations with different bottom friction (Manning) coefficients. We have always used Manning coefficient $n = 0.025$, a commonly used value for tsunami modeling, which is appropriate for gravelly earth.

- Tsunami model: The GeoClaw numerical model is thought to be suitably accurate, as discussed in Section 5. However, it does not solve the shallow water equations exactly and so the computed solutions have errors relative to the true solution of these equations. Moreover the shallow water equations are not a perfect model of the fluid dynamics, so even the exact solution of these equations would not agree with the actual inundation from the event being modeled. The errors introduced in modeling and numerical simulation can also be considered as uncertainties in the predicted inundation patterns. In principle one could attempt to include this uncertainty in a probabilistic model. For example, by studying the difference between numerical results and actual observations from many past events it might be possible to estimate the probability distribution of differences between the two. However, this is complicated by the fact that the earthquake source for past events is generally not known with great precision, so it is hard to separate the error due to the numerical model from the error due to the incorrect specification of the tsunami source.

  In this study we have not attempted to include uncertainty due to the mathematical or numerical model of the shallow water equations. However, we have done studies in which key parameters such as the mesh sizes have been varied in order to verify that our solutions are essentially converged. Together with past validation studies of various shallow water codes we feel fairly confident that the errors due to the modeling are relatively small compared to the uncertainty in the sources used.

5 The GeoClaw tsunami model

5.1 Overview of code and methods

The GeoClaw tsunami model is a branch of the Clawpack open source software package, and is available via the website www.clawpack.org/geoclaw. Clawpack (Conservation Laws Package) was first released by LeVeque in 1994 and the package has been extensively developed and improved over the years. Clawpack is a general package for solving linear and nonlinear hyperbolic systems of partial differential equations, including the important class of nonlinear conservation laws, whose solutions typically contain shock waves and other discontinuities. Robust shock capturing methods are used that are designed to handle strong shock waves. These methods are described in detail in [17].

GeoClaw was originally named TsunamiClaw and originated out of the PhD dissertation of David George [10], completed in 2006. The code has since been further developed for tsunami modeling, and has also been adapted to solve other geophysical flow problems using two-dimensional depth-averaged systems of equations.

For tsunami modeling, the two-dimensional shallow water equations (also called the St. Venant equations) are solved. This system of equations is commonly used for modeling tsunami propagation and inundation, and is also the system of equations solved by other models such as MOST [36].

The shallow water equations (SWE) are a nonlinear depth-averaged system of partial differential equations in which the fluid depth $h(x, y, t)$ and two horizontal depth-averaged velocities $u(x, y, t)$ and $v(x, y, t)$ are introduced. These equations are written in a form that corresponds to conservation of mass and momentum whenever the terms on the right hand side vanish:

$$\begin{aligned} h_t + (hu)_x + (hv)_y &= 0, \\ (hu)_t + \left(hu^2 + \frac{1}{2}gh^2\right)_x + (huv)_y &= -ghB_x - Dhu, \\ (hv)_t + (huv)_x + \left(hv^2 + \frac{1}{2}gh^2\right)_y &= -ghB_y - Dhv. \end{aligned} \tag{2}$$

Subscripts denote partial derivatives. The momentum source terms on the right hand side involve the varying bathymetry $B(x, y, t)$ and a frictional drag term, where $D(h, u, v)$ is a drag coefficient given by

$$D(h, u, v) = n^2 g h^{-4/3} \sqrt{u^2 + v^2}. \tag{3}$$

The parameter n is the *Manning coefficient* and depends on the roughness. For tsunami modeling a constant value of $n = 0.025$ is often used and we have adopted that value for much of this work, following standard practice.

Coriolis terms can also be added to the right hand side of equations (2), but these generally have been found to be negligible in tsunami modeling. We have performed some of our computations both with and without the Coriolis terms and have confirmed this for the case of inundation in Crescent City.

The finite volume methods implemented in GeoClaw are based on dividing the computational domain into rectangular grid cells and storing cell averages of mass and momentum in each grid cell. These are updated each time step by a high-resolution Godunov type method [17] that is based on solving Riemann problems at the interfaces between neighboring grid cells and applying nonlinear limiters to avoid nonphysical oscillations. These methods are second order accurate in space and time wherever the solution is smooth, but robustly handle strong shock waves and other discontinuous solutions. This is important when the tsunami reaches shallow water and hydraulic jumps arise from wave breaking.

The methods have been extended to also deal robustly with inundation. Grid cells where $h = 0$ represent dry land. Cells can dynamically change between wet and dry each time step. The grid resolution near Crescent City is taken to be sufficiently fine that the shoreline and edge of the inundated region can be well approximated by the edge of the wet region.

Block structured adaptive mesh refinement (AMR) is used to employ much finer grid resolution in regions of particular interest. Regions of refinement track the tsunami as it propagates across the ocean and then additional levels of refinement are added around the coast of California and in the Crescent City region. We typically use 6 levels of refinement going from a coarse grid with 2° resolution covering much of the Pacific Ocean on Level 1, to the finest Level 6 having resolution of 2/3" in the region shown in Figure 1.

5.2 Grid refinement studies

Some events have been simulated at two different grid resolution as a way to verify that the grid being used is sufficiently fine to capture a converged solution of the shallow water equations. Figure 6 shows one such comparison, in which the top row is computed with 2/3" resolution on the finest level (as has been done in our production runs). The results are then interpolated onto a 1/3" grid for plotting purposes and to compute the probabilistic results on this finer grid. The bottom row shows results if the finest level covering Crescent City is instead refined to 1/3". These results suggest that there would be little to be gained by solving on the finer grid.

5.3 Past validation studies

The GeoClaw model has undergone extensive verification and validation tests for tsunami modeling, as reported in [4, 6, 19, 11, 22, 18]. (*Verification* means confirming that the mathematical model equations are being solved correctly and accurately, while *validation* refers to investigating how well the solution of these equations agrees with reality.) Most of these papers and many simulation results can be found on the GeoClaw webpage, `http://www.clawpack.org/geoclaw`.

In particular, the GeoClaw model was extensively tested as part of a benchmarking workshop sponsored by the U.S. National Tsunami Hazard Mitigation Program (NTHMP) in 2011 [11, 28]. Nine tsunami benchmark problems were solved and the solutions compared at the workshop, and by the committee responsible for approving numerical models for NTHMP funded work. As a result of successful completion of the benchmark problems, the GeoClaw model has been approved by the NTHMP.

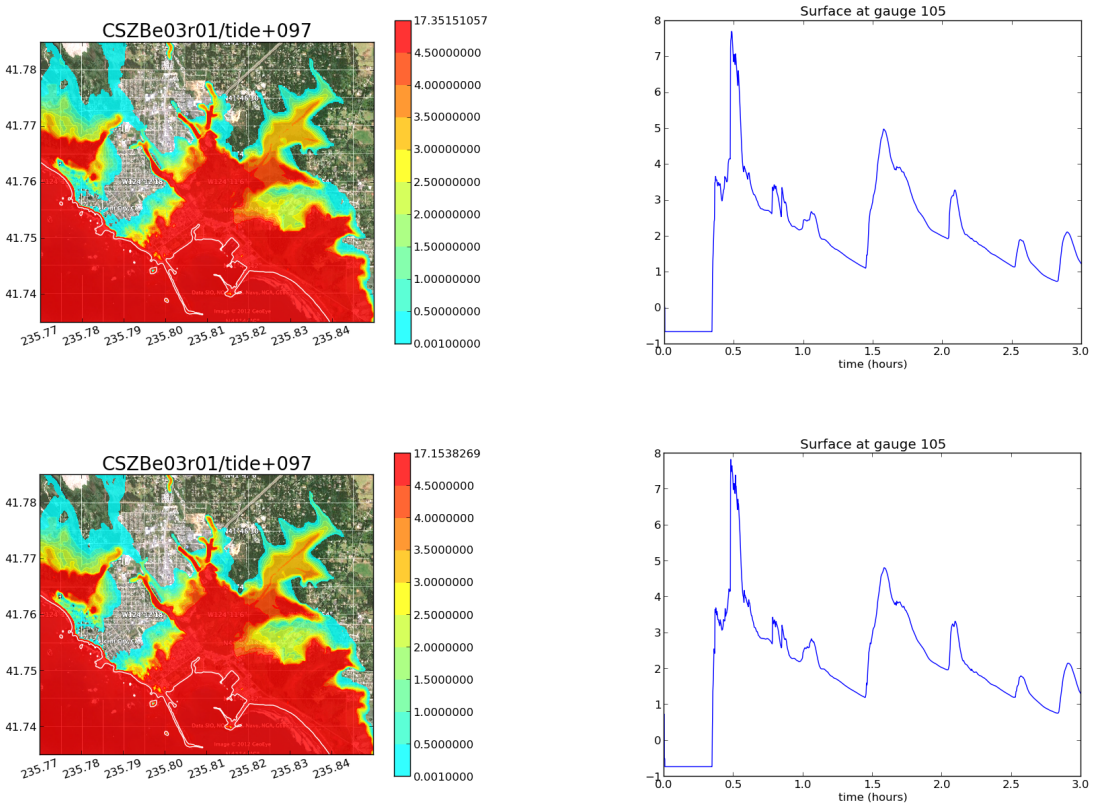

Figure 6: Results of one event realization CSZBe03r01 computed with two different fine grid resolutions. The top figures are using a 2/3" grid and the bottom is refined to 1/3". In each case the figure on the right is the depth as a function of time at gauge 105 from Figure 2.

The benchmarks included comparison to analytic solutions, wave tank experiments, and one historical event, the 1993 tsunami that struck Okushiri Island.

Data from the Tohoku event of 11 March 2011 have recently been used to further validate the GeoClaw model, funded in part by an NSF RAPID grant awarded for this purpose. In one study [22], ten different proposed tsunami sources were used together with GeoClaw tsunami modeling to compare against several sets of observations. Five DART buoys were considered, along with comparison of the computed and observed inundation on the Sendai Plain and at four other locations along the Sanriku Coast of Japan (north of Sendai). Comparisons of GeoClaw results to the observed tide gauge measurements in Crescent City during this event are shown in Figure 9 for one of these sources.

6 Validation results for Crescent City

In this section we present some sample results obtained for Crescent City, both to clarify the methodology used in this study and to further validate the code for this application. We illustrate results for two events. The first is the earthquake source AASZe03, a model for the 1964 Alaska earthquake that caused substantial flooding in Crescent City. The second is the 11 March 2011 Tohoku event, which caused substantial damage in the harbor but little flooding onshore.

6.1 Results for Alaska 1964

This earthquake source AASZe03 is discussed further in Section 7.1. It is a model for the 28 March 1964 event that flooded parts of the city, as illustrated in Figure 7.

Figure 8 shows the results of the GeoClaw simulation. The color map shows values of ζ, which is defined as elsewhere in this report to be the maximum flow depth over the full computation at points on land, or the maximum surface elevation relative to MHW for points offshore, measured in meters. In comparing these results to Figure 7, several points must be kept in mind:

- The true earthquake source for this 1964 event is not well understood. The source AASZe03 is an approximation based on a crude model in which the roughly 600×100 km fault geometry was split into 12 rectangular fault segments (100×50 km each) and a uniform slip imposed on each. See Section 7.1 for more details. Because this may not be a good approximation to the true seafloor motion, it is not clear how well the simulated inundation should match the true inundation.

- The blue line in Figure 7 is the approximate inundation limit, but it is not known how accurate this is. In particular, in the Elk Creek valley the inundation does not appear to go nearly as far inland in this map as in the GeoClaw simulation, but this area is largely uninhabited and and it is not known how much effort was made to map this region.

- The Crescent City bathymetry has changed since 1964. In particular, the marina in our bathymetry did not exist in 1964.

In spite of these limitations, the inundation of the downtown region appears to be quite similar to that shown in Figure 7.

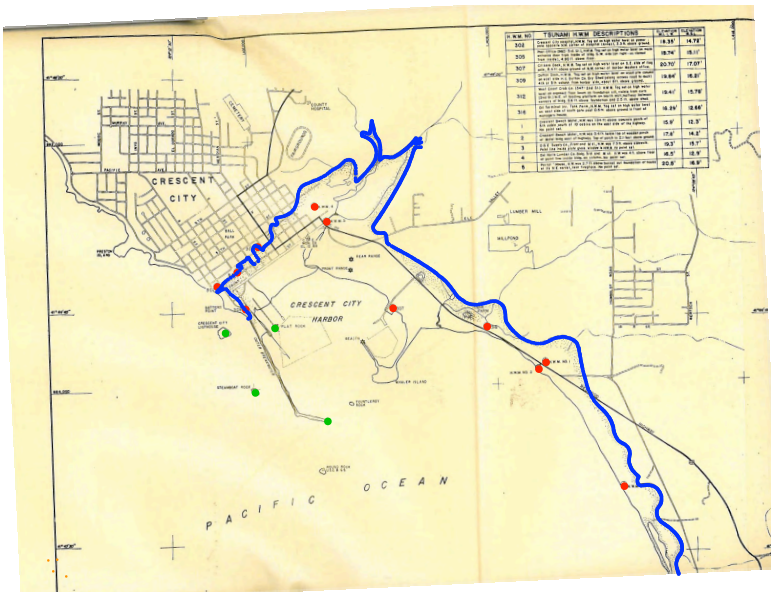

Figure 7: Inundation limits of the 1964 Alaska event tsunami, see Magoon [23].

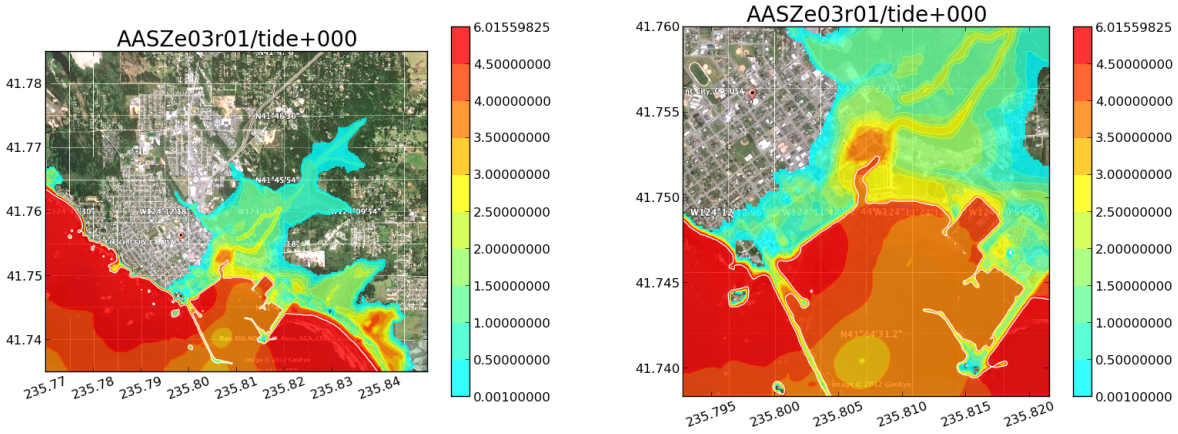

Figure 8: GeoClaw simulation results for the AASZe03 source, modeling the 1964 event. Left: full region where maximum inundation is recorded over each run on a 1/3" grid. Right: zoom of the harbor and downtown area. The run at MSL is shown.

6.2 Results for Tohoku 2011

Figure 9 shows observations at the tide gauge in Crescent City Harbor during the 11 March 2011 Tohoku tsunami (after de-tiding), compared with results from a GeoClaw simulation, along with the simulated inundation. This run was at MLW since the main waves hit at low tide, and was performed using the source model from G. Shao, et. al. [35]. MacInnes et al. [22] compared this source model to 9 others, and found that this one gave good agreement with many observations of both DART buoys and inundation along the coast of Japan. This is the source denoted TOHe01 in our probabilistic study, as discussed further in Section 7.5.

Wilson, et. al. [39] report that the Crescent City harbor experienced a maximum tsunami wave height of about 2.5 meters, and that the small boat harbor was nearly completely destroyed, at a cost of $20M. In spite of this loss, however, they report that significant runup did not occur.

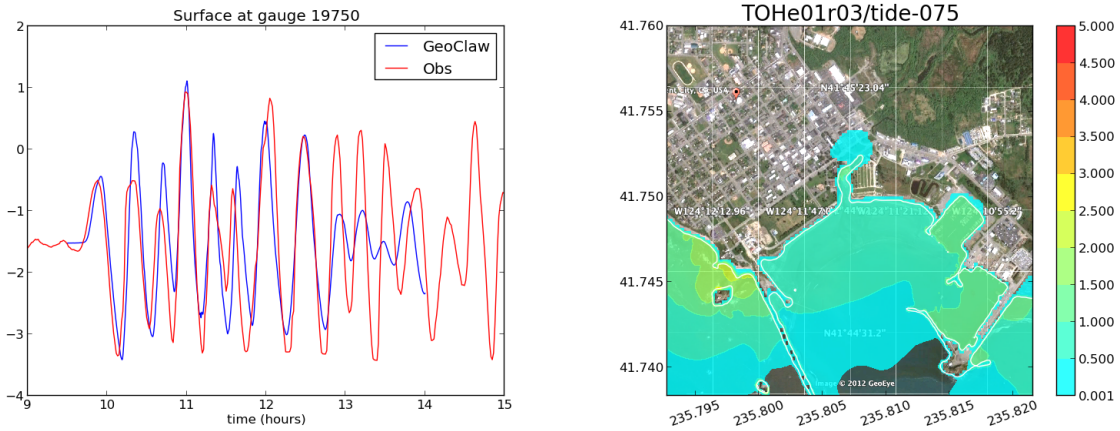

Figure 9: GeoClaw simulation of the 11 March 2011 Tohoku event using the TOHe01 source from [35] . Left: Tide gauge 19750 in Crescent City Harbor. Observations are shifted by 10 minutes. Right: maximum inundation ζ.

7 Earthquake sources used for this study

Far-field sources used in this study, with the exception of sources off Japan, are those listed in Table 1 of the Seaside, OR, PTHA study (Tsunami Pilot Study Working Group (TPSWG), González, et al., [14]). The 2011 Tohoku event devastated the Japanese coast and inflicted serious damage on the coast of California, with more than $50-million in damage to two dozen harbors and one fatality (Wilson [38]). Consequently, a far-field source off Japan was also developed for this study as described below.

Near-field source specification in the Cascadia Subduction Zone was more difficult. Details of the incident wave characteristics, which are determined by the spatial structure of the seismic crustal displacement, have a strong effect on the degree of coastal inundation; this means a stochastic approach must be employed in which multiple realizations of the seismic slip distribution are generated, subject to geophysical constraints. It is the specification

Table 1: Study Source Parameters. The slip values for AASZ06-08, KmSZe01-02, KrSZe01-03, and SChSZe01 are corrections to the values used in the Seaside study of González, et.al. [12]. The conditional probabilities (weights) used in the analysis are 1 for the events with only one realization, and are given in the Total Weight column of Table 3 for the CSZBe01r01-CSZBe01r15 realizations in Figure 16.

Source Name	M	Length (km)	Width (km)	Slip (m)	T_M (yr)	Fault Model Specification
AASZe01	9.2	1000	100	17.7	1313	acsza9-18, acszb9-18 (Model 1 West)
AASZe02	9.2	1000	100	17.7	750	acsza19-28, acszb19-28 (Model 1 Mid)
AASZe03	9.2	600	100	Dist.	750	acsza31-36, acszb31-36 (Model 1 East)
AASZe04	9.2	1200	100	14.8	1133	acsza11-22, acszb11-22 (Model 2 West)
AASZe05	9.2	1200	100	14.8	750	acsza23-34, acszb23-34 (Model 2 East)
AASZe06	8.2	300	100	1.9	875	acsza28-30, acszb28-30 (Model 3 West)
AASZe07	8.2	300	100	1.9	661	acsza31-33, acszb31-33 (Model 3 Mid)
AASZe08	8.2	300	100	1.9	661	acsza34-36, acszb34-36 (Model 3 East)
KmSZe01	8.8	500	100	8.9	100	kisza1-5, kiszb1-5
KmSZe02	8.8	500	100	8.9	100	kisza6-10, kiszb6-10
KrSZe01	8.5	300	100	5.3	500	kisza11-13, kiszb11-13
KrSZe02	8.5	300	100	5.3	500	kisza14-16, kiszb14-16
KrSZe03	8.5	300	100	5.3	500	kisza17-19, kiszb17-19
SChSZe01	9.5	1100	100	45.3	300	sasza39-49, saszb39-49
TOHe01	9.0	500	200	Var.	103	Shao, et.al. [35]
CSZBe01r01-CSZBe01r15	Var.	1000	Var.	Var.	332	Witter, et.al [40]

of these geophysical constraints on the slip distribution that is problematic, and this is discussed in more detail, below. After much discussion with experts, we decided to use the 15 realizations of CSZ events developed for a recent study of Bandon, OR [40]. These are discussed further in Section 7.6.2.

Detailed descriptions and justifications of our far-field sources also used in the Seaside study are provided in the TPSWG (2006) report [14]. In general, to take advantage of previous work in determining likely source parameters, these source specifications follow similar efforts used in the National Seismic Hazard Mapping Program. Note that, as in the Seaside study, only the largest earthquakes that might occur are considered because, although the recurrence rates are low, inclusion of more frequent but smaller earthquakes (and the associated tsunamis) is not likely to affect the 100- and 500-year hazard curves of interest. Table 1 lists the source parameters for our sources. Note that the Fault Model Specification column identifies the individual fault planes of the PMEL Unit Source Database as referenced in Arcas and Uslu [3]. Most of the text in the next four sections that explain the entries in Table 1 is taken verbatim from TPSWG [14].

7.1 Alaska Aleutians Subduction Zone (AASZ)

The seismic hazard maps for Alaska are described by Wesson et al. (1999), who consider two hazard models (Models I and II) for the Alaska-Aleutian megathrust in which earthquakes as large as M = 9.2 can occur. Model I consists of a western and an eastern seismic zone. The delineation between the zones occurs approximately at the site of the 1946 Aleutian

earthquake. Model II consists of a western Aleutian seismic zone (Zone A) as in Model I, but a smaller eastern Alaska seismic zone with a western boundary coincident with the rupture boundary for the 1964 earthquake. The first tsunami model consists of three M = 9.2 earthquakes (West, Middle and East), with adjacent rupture areas. The East M = 9.2 ruptures would correspond in location to the 1964 rupture, whereas the West and Middle rupture areas would not correspond to any historic event. The Middle event also spans what some may believe is a tectonic segment boundary at the tip of the Alaska Peninsula. It is important that the rupture areas for the three events do not overlap as this would violate an important seismic moment balance along the subduction zone. Model III (West, Middle and East) was added to accommodate the possibility that a smaller magnitude earthquake (M = 8.2) in Prince William Sound might cause larger inundation at Crescent City than other earthquakes considered in this initial set of source parameters. Figures 10 and 11 present the slip and seafloor deformation for each of these earthquake source models.

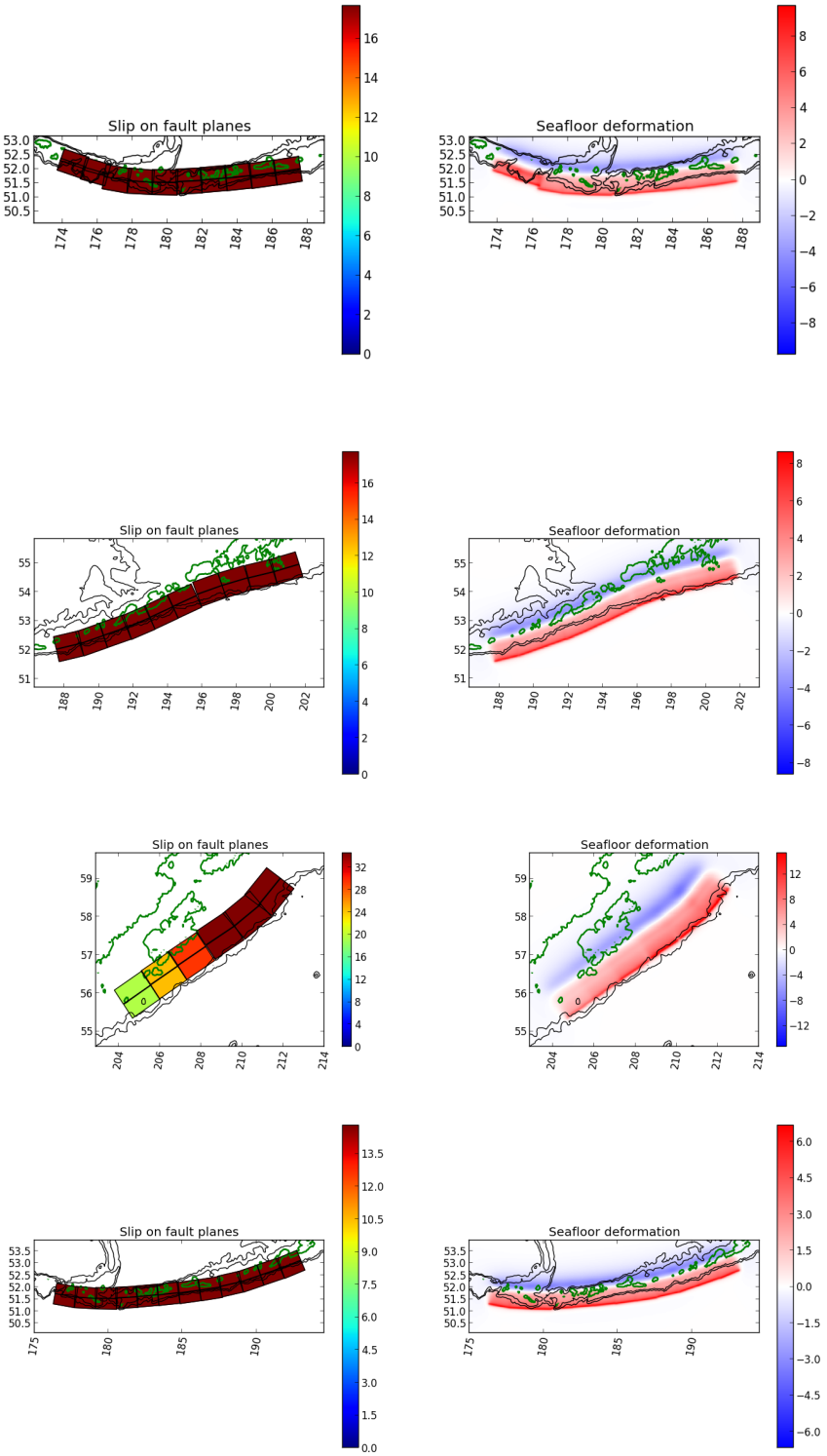

Figure 10: The sources AASZe01 through AASZe04. Left: slip on fault plane. Right: Resulting seafloor deformation. Note: AASZe03 is the only one in which the slip varies spatially, and is a model for the 1964 Alaska event.

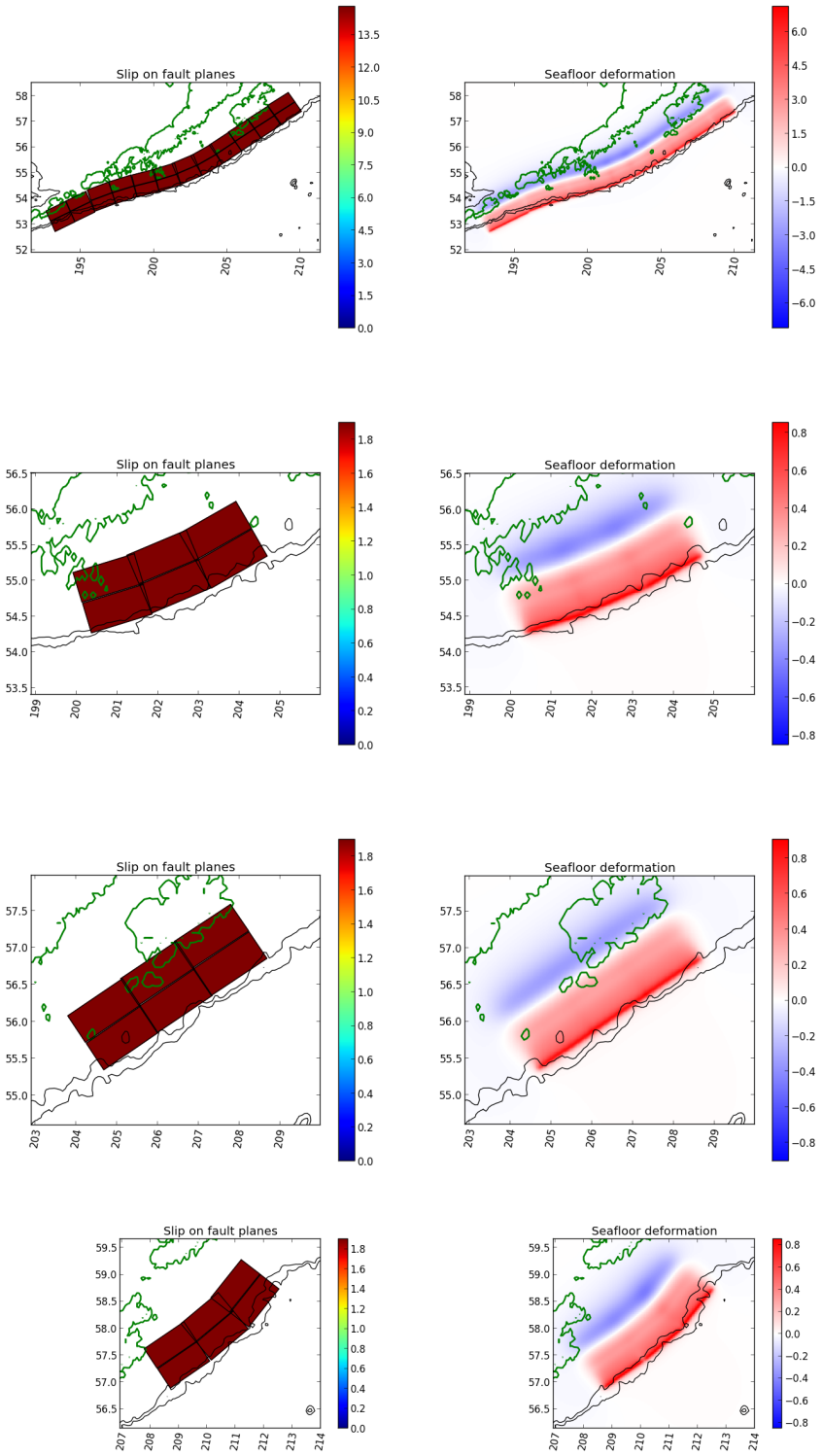

Figure 11: The sources AASZe05 through AASZe08. Left: slip on fault plane. Right: Resulting seafloor deformation.

7.2 Kamchatka Subduction Zone (KmSZ)

Like the Alaska-Aleutian Subduction Zone, large earthquakes have occurred along the Kamchatka Subduction Zone (KSZ) with noticeable frequency. Pinegina et. al. [30] concluded that Kamchatka has been impacted by large tsunamis at a rate of 1 every 100 years for the past 3,000 years, though not all are from local sources (about 10-20% are far field). Of note, the Mw = 8.8 1952 (Johnson and Satake, [16]) and the Mt = 8.8 1923 [1] earthquakes are probably representative of the largest earthquakes of this subduction zone. A tsunami model for Kamchatka can be constructed as done for the Alaska Tsunami Model 1 above, with two adjacent M = 8.8 earthquakes filling the entire subduction zone. Figure 12 presents the seafloor deformation for each of these earthquake source models.

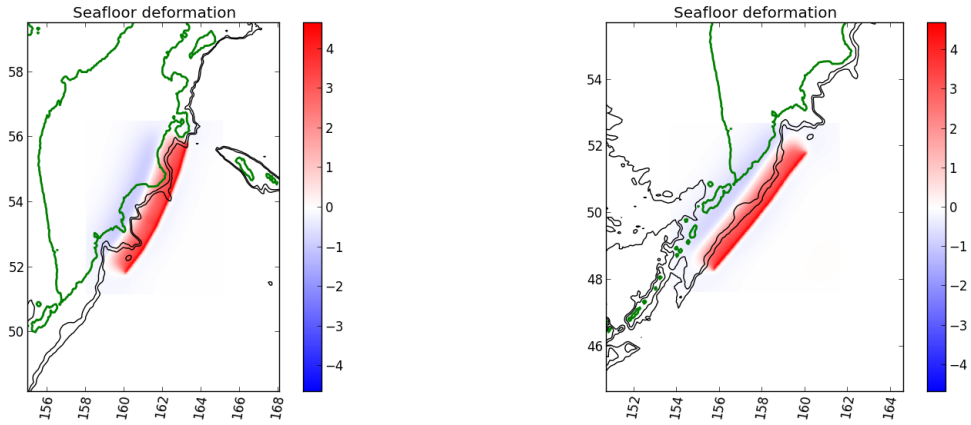

Figure 12: Seafloor deformation for the sources KmSZe01 and KmSZe02.

7.3 Kurils Subduction Zone (KrSZ)

Continuing south along the Kuril Subduction Zone, the maximum magnitude earthquake is likely to be slightly smaller than for the Kamchatka Subduction Zone, primarily because of a change in tectonic regime for the overriding plate. From the analysis of the 13 October 1963 Kuril Islands earthquake (there was also a tsunami earthquake in the Kuril Islands on 20 October 1963) which Ward [37] and Ruff and Kanamori [32] placed at Mw = 8.5 and recent evidence of multi-segment rupture in the southern part of the Kuril Subduction Zone by Nanayama et. al. [27], it is reasonable to characterize this subduction zone with a series of M = 8.5 earthquakes. Nanayama et. al. [27] indicates that the average return time for these earthquakes is approximately 500 years. Approximately three M = 8.5 earthquakes would fill the Kuril Subduction Zone up to the southern extent of the Kamchatka Subduction Zone. Figure 13 presents the seafloor deformation for each of these earthquake source models.

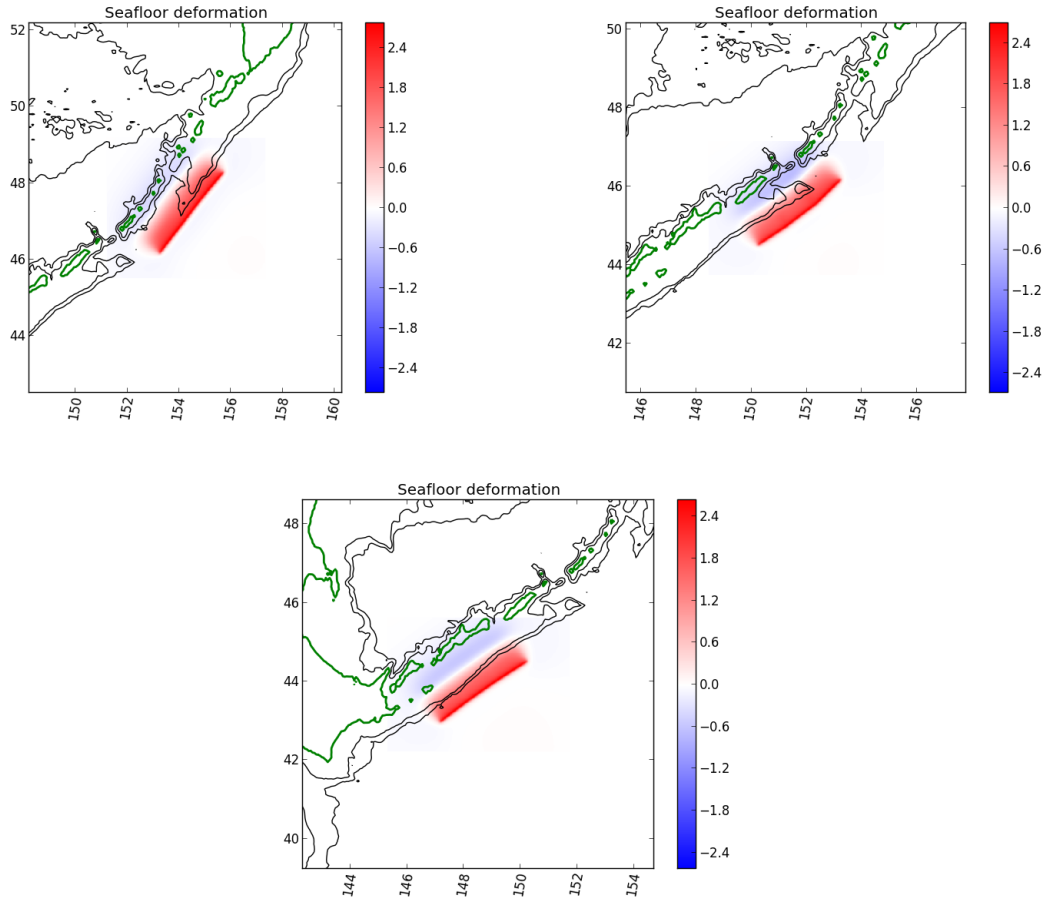

Figure 13: Seafloor deformation for the sources KrSZe01, KrSZe02 on the top and KrSZe03.

7.4 South Chile Subduction Zone (SChSZ)

Earthquakes along the Chilean Subduction Zone are also considered, primarily because of the size of the M = 9.5-9.6 1960 earthquake (Cifuentes, [8]; Cifuentes and Silver, [9]) and observations of the associated tsunami along the west coast of North America. The amount of slip that occurred during the 1960 tsunami is difficult to ascertain because of the complexity of the event. The geodetic models of both Linde and Silver [20] and Barrientos and Ward [5] result in average amounts of slip that correspond to significantly lower seismic moment estimates than determined from seismic waveform data, though still at M about the 9.5 level. Average slip estimates vary from 17 m to 20 m, though the variable slip models indicate significantly higher amounts of slip, as much as 40-50 m, are predicted for the off shore extent of rupture and even small earthquakes (Barrientos and Ward, [5]; Linde and Silver, [20]). For comparison, Liu et. al. [21] use 24 m of slip in their far-field tsunami model.

Chile has been struck by giant earthquakes and tsunamis in the past, including the 1570s, 1730s, 1837, and the M about 9.5 1868 earthquake in northern Chile. These dates are not representative of return times for M about 9.5 earthquakes from purely a moment-balance perspective (Barrientos and Ward, [5]) and from recent paleoseismologic analysis by Salgado et. al. [33]. The latter study suggests an average return time for great earthquakes in Chile of about 250 years. Even so, if the average slip per event is about 20 m, this results in a seismic slip rate of 8 cm/yr or close to the relative plate convergence rate of 8.4 cm/yr. Although the southern Chile Subduction Zone is considered the most highly coupled subduction zone in the world in terms of seismic efficiency (Scholz, [34]), the repeat time should not be much smaller, nor the average slip per event be much greater, than these estimates to satisfy the moment balance. Figure 14 presents the seafloor deformation for each of these earthquake source models.

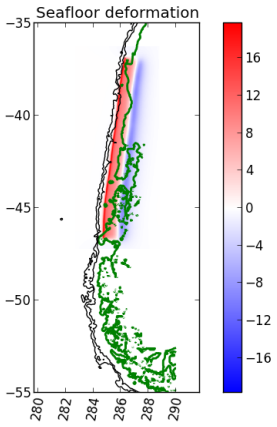

Figure 14: Seafloor deformation for the source SChSZe01.

7.5 Japan

The far-field sources in the Seaside study did not include potential sources offshore Japan. However, the 11 March 2011 Tohoku M9 earthquake and associated tsunami devastated the Japanese coast, leading us to include such an event in this study as a potential far-field source. Many different sources have been proposed for this event and a comparison of 10 of these sources as input to the GeoClaw model has been performed in [22]. The sources all gave consistent results with observations, both at DART buoys and at several regions on the Japan coast where inundation was compared. Any one of these sources could be used as a potential Japan source for the present study, and we have chosen to use the one proposed by G. Shao, et. al. [35], as discussed further in Section 6.2.

This is not the only possible event on the Japan trench, but we have been unable to obtain good slip realizations for other possible events. Instead we will use the Tohoku event as a proxy for an event originating anywhere in this region, and set the recurrence time to $T_M = 103$ years. This is the mean return time for a similar earthquake to occur somewhere along the Japan Trench faults, as estimated by the Japan Earthquake Research Center (JERC) in their online summary of Japanese earthquakes, see [15]. Because this fault region is so far removed from Crescent City, we believe that the inundation will be little affected by the details of location, and the Tohoku event is thought to be among the worst possible in terms of concentrated slip distribution and resulting tsunami magnitude. Even so it results in very little inundation and hence has little effect on the resulting probabilistic results.

7.6 Cascadia Subduction Zone (CSZ)

The Cascadia Subduction Zone (CSZ) extends from Northern California to Vancouver Island and is known to have produced earthquakes of magnitude 9.1 or greater in the past. Extensive paleaotsunami records indicate that many events over the past several thousand years have led to extensive inundatation all along the coast and in particular in the area surrounding Crescent City. However, there have been no major events in recorded history, other than the Mw 9.1 event of 1700 for which observations are available only in Japan. From the geologic record it is difficult to estimate the range of possible events that may occur in this zone or to accurately estimate return times. This means that there is a great deal of epistemic uncertainty associated with CSZ.

Because this subduction zone is so long ($\approx$ 1100 km) and the southern extent lies directly offshore Crescent City, the details of how slip is distributed over the fault zone have a much greater impact on the resulting inundation than is the case with farfield earthquake sources. This suggests that a large number of realizations may be necessary in order to adequately explore the aleatoric uncertainty, even if the epistemic uncertainties could be eliminated. This means that the probability distribution of possible events (even if known exactly) would lie over a relatively high dimensional stochastic space compared to farfield sources. Techniques that might be further developed to efficiently explore this space are briefly discussed in Section 10.2.

The combination of large epistemic uncertainty and high-dimensional stochastic space lead to identifying the choice of CSZ source realizations as the most questionable aspect of

the current study and the most important source of uncertainty in the probabilistic results.

7.6.1 Recurrence time for CSZ Mw 9.1

Although the recurrence time for a CSZ Mw 9.1 event is thought to be around 525 years, the fact that the last event was in 1700 leads seismologists to believe the next such event may happen sooner than would be predicted by a Poisson process with rate $\nu = 1/525$. In [29] it was estimated that there is a 14% probability of such an event in the next 50 years. From this we can deduce that a good approximation would be to assume it is a Poisson process going forward with rate $\nu \approx 1/332$, and so we have used a recurrence time of 332 years in our study. This is based on setting $1 - e^{-50\nu} = 0.14$ and solving for ν, and corresponds to an annual probability of occurrence $p = 1 - e^{-\nu} \approx \nu$.

7.6.2 Bandon study sources

Based on an analysis of paleoseismic data, including turbidite records, Witter, et. al. [40] generated rupture models for Cascadia Subduction Zone earthquakes to conduct a study of tsunami inundation at Bandon, Oregon. The fault parameters, including estimates of the average recurrence interval, are summarized in Table 4 of their report, which is reproduced in Figure 16. A DVD of vertical seafloor deformation data files for each of these models can be ordered online from the Nature of the Northwest (http://www.naturenw.org/). These sources are based on a logic tree formulation as illustrated in Figure 7 of [40], which is reproduced in Figure 15.

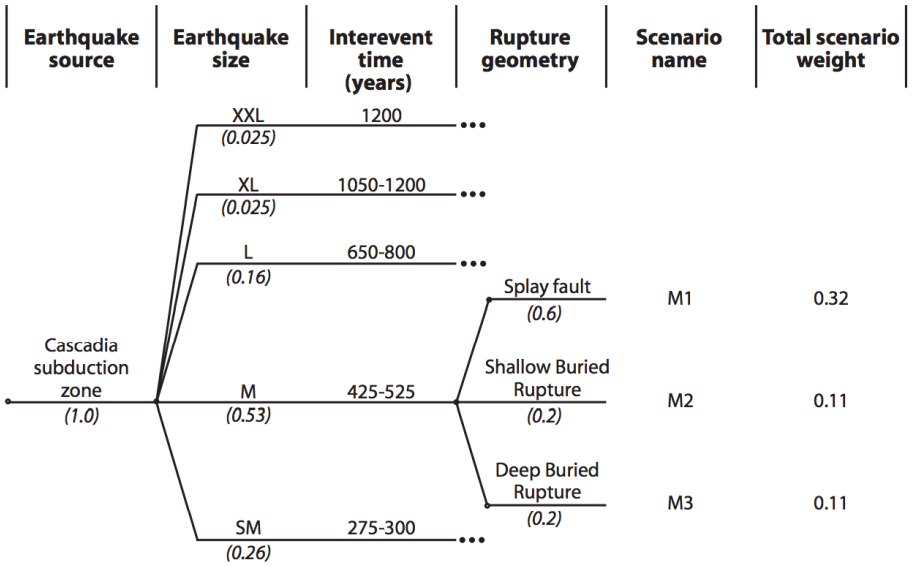

Figure 15: Figure 7 from [40], which illustrates the logic tree used to assign conditional probabilities to different realizations of 5 possible CSZ events (in our terminology).

Figure 17 and Figure 18 show the seafloor deformation for these sources. We assume these 15 sources are realizations of a single event, and we run two sets of probabilistic

Table 3. Cascadia earthquake source parameters used to define 15 rupture scenarios. Logic tree branch weights shown in parentheses. Total scenario weight listed in right column.

Earthquake Size	Interevent Time (yrs)	Fault Geometry	Slip Range (m)		M_w	Scenario Name	Total Weight
			Maximum	Average			
Extra Extra Large (0.025)	1,200	Splay fault (0.8)	36–44	18–22	~9.1	**XXL 1**	0.02
		Shallow buried rupture (0.1)	36–44	18–22	~9.2	**XXL 2**	0.0025
		Deep buried rupture (0.1)	36–44	18–22	~9.1	**XXL 3**	0.0025
Extra Large (0.025)	1,050–1,200	Splay fault (0.8)	35–44	17–22	~9.1	**XL 1**	0.02
		Shallow buried rupture (0.1)	35–44	17–22	~9.2	**XL 2**	0.0025
		Deep buried rupture (0.1)	35–44	17–22	~9.1	**XL 3**	0.0025
Large (0.16)	650–800	Splay fault (0.8)	22–30	11–15	~9.0	**L 1**	0.128
		Shallow buried rupture (0.1)	22–30	11–15	~9.1	**L 2**	0.016
		Deep buried rupture (0.1)	22–30	11–15	~9.0	**L 3**	0.016
Medium (0.53)	425–525	Splay fault (0.6)	14–19	7–9	~8.9	**M 1**	0.318*
		Shallow buried rupture (0.2)	14–19	7–9	~9.0	**M 2**	0.106
		Deep buried rupture (0.2)	14–19	7–9	~8.9	**M 3**	0.106
Small (0.26)	275–300	Splay fault (0.4)	9–11	4–5	~8.7	**SM 1**	0.104
		Shallow buried rupture (0.3)	9–11	4–5	~8.8	**SM 2**	0.078
		Deep buried rupture (0.3)	9–11	4–5	~8.7	**SM 3**	0.078

*Scenario M1 carries the highest weight and represents the "most likely" event in our analysis.

Table 4. Estimated earthquake magnitudes for Cascadia rupture scenarios

Rupture Scenario	Length (km)	Width (km)[a]	Interevent Time (yrs)	Maximum Slip (m)[b]	Average Slip (m)[c]	Seismic Moment (10^{22} N m)[d]	Moment Magnitude (M_w)[e]
XXL1	1,000	83	1,200	41	20	6.6	9.1
XXL2	1,000	105	1,200	41	20	8.4	9.2
XXL3	1,000	83	1,200	41	20	6.6	9.1
XL1	1,000	83	1,200	41	20	6.6	9.1
XL2	1,000	105	1,200	41	20	8.4	9.2
XL3	1,000	83	1,200	41	20	6.6	9.1
L1	1,000	83	800	27	13	4.4	9.0
L2	1,000	105	800	27	13	5.6	9.1
L3	1,000	83	800	27	13	4.4	9.0
M1	1,000	83	525	18	9	2.9	8.9
M2	1,000	105	525	18	9	3.7	9.0
M3	1,000	83	525	18	9	2.9	8.9
SM1	1,000	83	300	10	5	1.7	8.7
SM2	1,000	105	300	10	5	2.1	8.8
SM3	1,000	83	300	10	5	1.7	8.7

[a]Equivalent fault width; modeled fault width varies with latitude.
[b]Maximum slip estimates are the product of the recurrence interval times a convergence rate at southern Oregon latitudes (34 mm yr^{-1}).
[c]Average slip estimate is 0.49 of maximum slip estimate.
[d]Seismic moment (M_0) = fault area × slip × rigidity, where rigidity = 4×10^{10} N m^{-2}.
[e]Moment magnitude (M_w) = (log M_0 – 9.1)/1.5.

Figure 16: Tables 3 and 4 from [40], listing the different CSZ events and realizations used in the study of Bandon, Oregon. For our study, we view this as one CSZ event with 15 different realizations with conditional probabilites given in the Total Weight column of Table 3.

computations that differ only in the assumed mean recurrence times of 332 and 525 years, with each assigned conditional probabilities based on the expert opinion of the Bandon study authors, as expressed in the "Total Weight" column of their Table 3, reproduced in Figure 16.

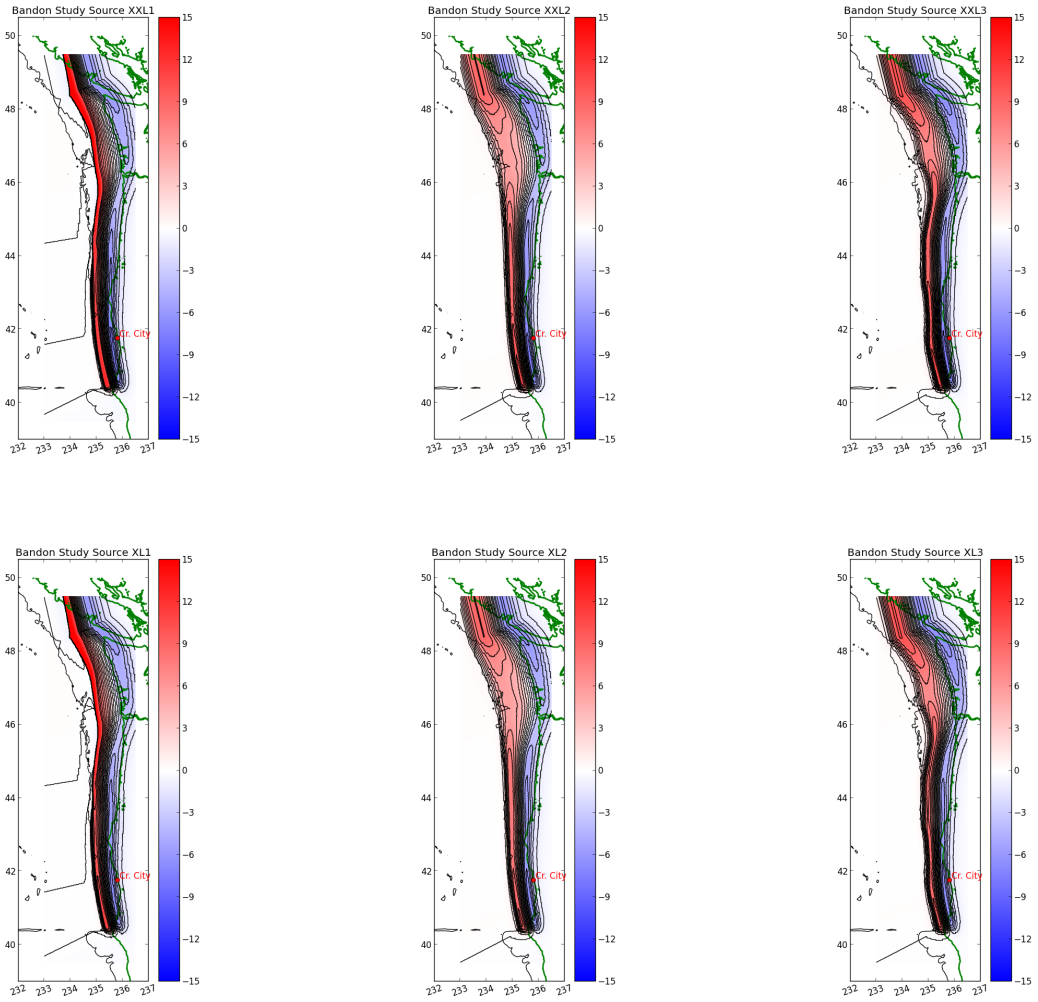

Figure 17: Seafloor deformation for the Bandon study sources [40]. Three realizations are given for each size XXL (top) and XL (bottom). Contours at 2 m increments.

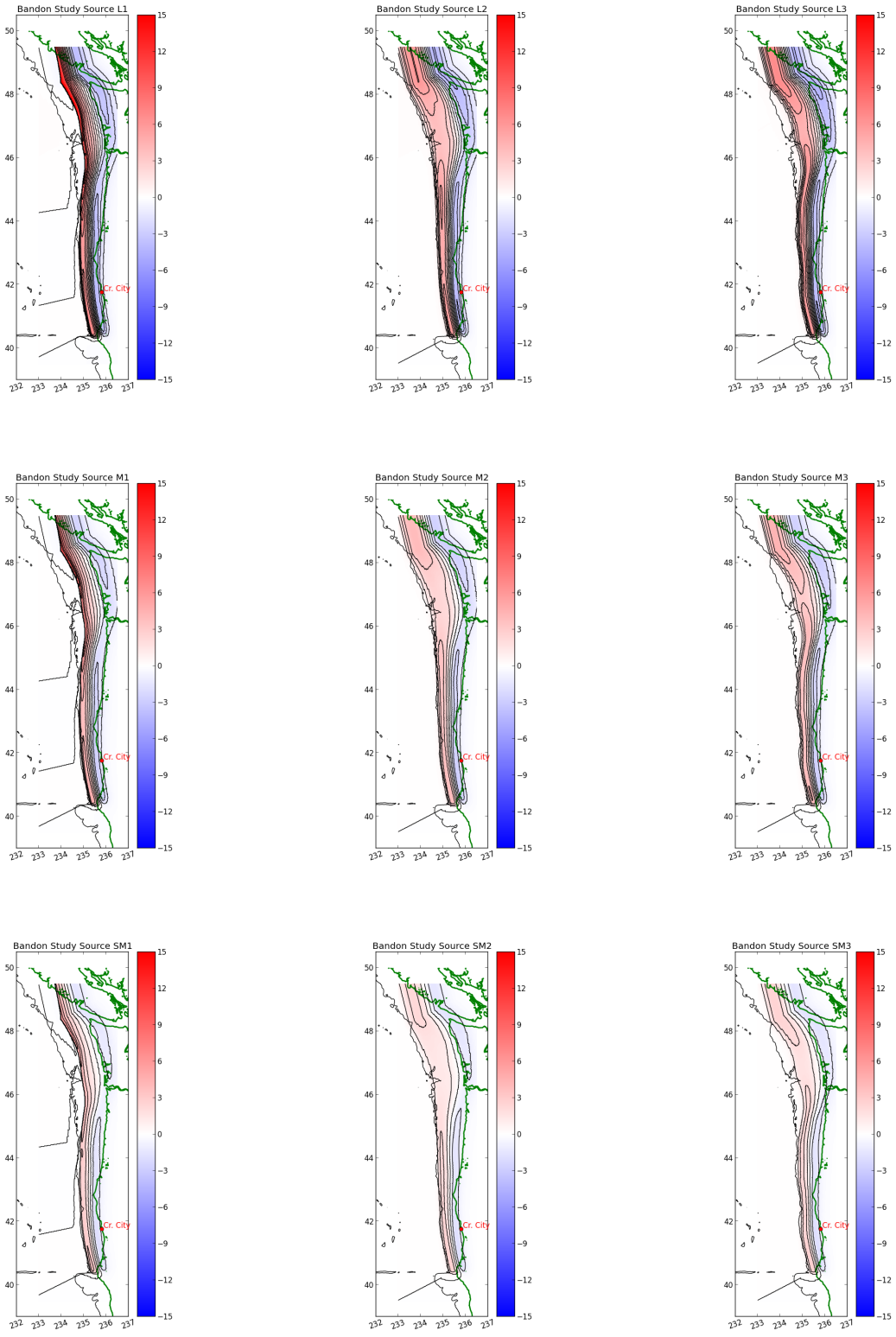

Figure 18: Seafloor deformation for the Bandon study sources [40]. Three realizations are given for each size L (top), M (middle), and SM (bottom). Contours at 2 m increments.

8 Overview of tidal uncertainty

The GeoClaw code is not modeling the tidal dynamics (i.e. the rise or fall of the tide within a single simulation, or how tidal currents could effect the inflow of the tsunami wave.) This limitation might be important to address and is a potential R&D topic. In this section, we present two new methods for incorporating the tidal effects as best we can given this limitation. Refer to Appendix B where we describe how we compute the probability of exceeding prescribed ζ levels.

The key ideas are the following:

- A tsunami wave that arrives at high tide will cause more flooding than the same wave arriving at low tide. But nonlinearities in the governing equations mean that there will be nonlinearities in the tsunami-tide interaction. For example, if the tide stage is 1 meter higher, the resulting maximum flow depth at a point will not generally be exactly 1 meter higher, even at points that are inundated at both tide levels.

- The GeoClaw code can easily be set to run with different (static) values of sea level in order to explore how the tide stage affects the level of inundation. The tide stage used for a run will be denoted by ξ, relative to MSL.

  For each exceedance level ζ_i and each grid point (x, y), we can use multiple GeoClaw runs to estimate how high the tide stage must be in order to observe a maximum flow depth above ζ_i at this point. This value of tide stage that must be exceeded will be denoted by $\xi = w_e$ below, the "water level to exceed". Note that w_e is different for each ζ_i at each (x, y) but in the discussion below we focus on a single point and exceedance level.

- We can then ask what the probability is that the tide stage will be above w_e when the tsunami arrives. If the tsunami consisted of a single wave of short duration, then the probability of exceeding ζ_i for this one realization would simply be the probability that the tide stage ξ is above w_e at one random instant of time i.e. a random point in the tide cycle. This can be estimated based on the past history of tides at Crescent City, as explained further below.

- However, it is not this simple because most tsunamis consist of a sequence of waves that arrive over the course of several hours. During this time the tide may rise or fall considerably. If the tsunami consists of a sequence of closely spaced and equally large waves arriving over a period of Δt hours, then the better question to ask would be: what is the probability that the tide stage will be above w_e at *any* time between t_0 and $t_0 + \Delta t$, where t_0 is a random time. For fixed Δt this can also be determined from past tide tables. This approach is explained further below as the "dt-method". Different events will require different choices of Δt. For example, a CSZ event typically gives one very large wave that causes most of the inundation. On the other hand farfield events may lead to a larger number of waves that arrive over many hours due to reflections from various distant points, any one of which could give flooding exceeding ζ_i if the tide stage is above w_e.

- For some events, it may be that there are several such waves separated by many hours when no waves arrive that could cause the same level of flooding. In this case choosing a large Δt may overestimate the probability of inundation above ζ_i. Instead we might want to specify a *pattern* of times specific to one realization when the dangerous waves arrive. For example, if the tsunami consists of two large waves of the same amplitude arriving 4 hours apart, the pattern might consist of a 1-hour window starting at time t_0 and another 1-hour window starting 4 hours later. We could then ask what the probability is that the tide stage will be above w_e at any time in this pair of windows, when t_0 is a random point in the tide cycle. This can also be determined based on the tide record and gives a smaller (and more accurate) probability than simply looking at a $\Delta t = 5$ hour window would. Similar questions can also be answered when the tsunami consists of multiple waves of different amplitudes. This is the basis of the "pattern method" described below.

- The dt and pattern methods were designed to use GeoClaw simulation information at multiple but static tidal levels. These methods will work with other simulation codes that have the capability to produce similar results.

8.1 Crescent City Tides

The tidal gauge at Crescent City (Gauge No. 9419750) has the following values for Mean Low Low Water (ξ_{MLLW}), Mean Low Water (ξ_{MLW}), Mean Sea Level (ξ_{MSL}), Mean High Water (ξ_{MHW}), and Mean High High Water (ξ_{MHHW}), respectively. In addition, we include the Lowest (ξ_{Lowest}) and Highest ($\xi_{Highest}$) water seen at the gauge in a year's data from July 2011 to July 2012. Unless explicitly stated, the tide levels we use are referenced to MSL.

Level	**Referenced to MSL**
ξ_{Lowest}	-1.83
ξ_{MLLW}	-1.13
ξ_{MLW}	-0.75
ξ_{MSL}	0.00
ξ_{MHW}	0.77
ξ_{MHHW}	0.97
$\xi_{Highest}$	1.50

Table 2: Crescent City tide values values, measured in meters relative to MSL.

A fixed number of bins is made from tide levels $-1.83 \leq \xi \leq 1.50$. Then the yearly tide data at Crescent City is associated with the appropriate bin to make the probability density function and associated cumulative distribution function shown in Figure 19. In the cumulative distribution plot, the horizontal axis represents tidal level and the vertical axis the probability of exceedance of this level at any point in time.

As mentioned in Appendix B, in order to add tidal uncertainty, we must be able to find the probability that the inundation height ζ exceeds each particular level ζ_i given that an event (or a realization of an event) actually occurs. In the sections below, we outline how

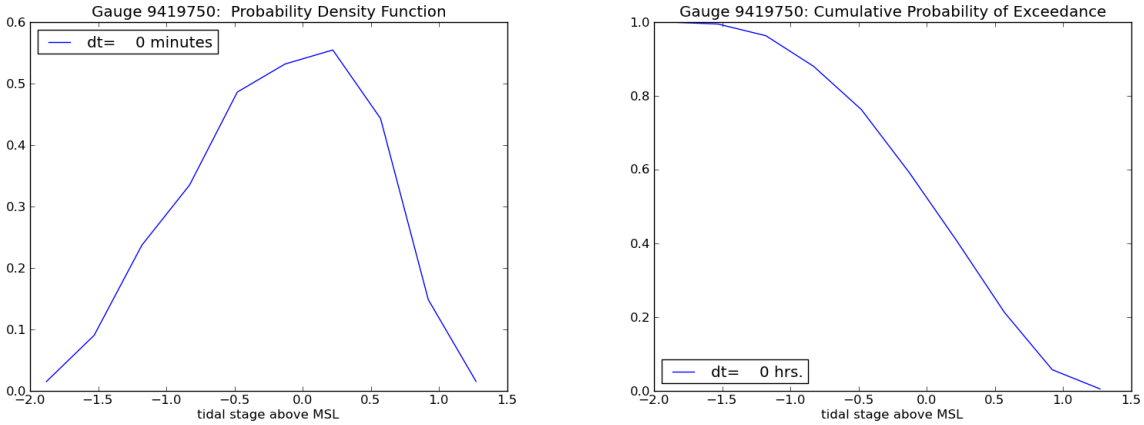

Figure 19: Crescent City Tidal Distributions (July 2011 - July 2012) Left: Probability Density Function (mean=0.0, $\sigma = .638$) Right: Cumulative Distribution Function

we find $P(\zeta > \zeta_i \,|\, E_{jk})$, the conditional probability of exceedance given that realization k of event j has occurred.

8.2 The dt-Method

For each E_{jk}, we run GeoClaw simulations at multiple tide levels, typically the three levels ξ_m for $m =$ MLW, MSL, and MHHW. We say tide level ξ_m produced the maximum GeoClaw inundation depth $\zeta(\xi_m)$ and plot the results as a piecewise linear function, as shown in the upper plot of Figure 20 below. (This is illustrated for a case where 7 tide levels ξ_m were run.) The intersection of the vertical dotted line with the tide level axis will give the minimum *static* tide level $\xi = w_e$ that could be used with GeoClaw in order to produce inundation depth $\zeta = \zeta_i$. Hence, if tide level $\xi > w_e$ were used for a GeoClaw run, we claim that $\zeta > \zeta_i$ would result.

If the horizontal dashed line in the upper plot of Figure 20 (at inundation level ζ_i) intersects the graph in multiple places (as would happen for example if inundation does not occur until the tide reaches a partiular level), we choose $\xi = w_e$ to be the smallest tide level above which ζ_i is exceeded. As an example, if $\zeta_i = 0$, the graph shows we only exceed ζ_i if the tide is above the third blue dot, so the tide level associated with the third data point would be chosen for w_e. It could also happen that the ζ_i inundation dotted line falls below the entire graph (think of shifting the graph up by .5 meters and considering $\zeta_i = 0$). In this case the probability is taken as 1 for exceeding ζ_i. Likewise, if the ζ_i inundation dotted line is above the entire graph, then ζ_i has probability of 0 of being exceeded. If w_e is greater than or equal to the highest tide possible at the Crescent City gauge, ζ_i can never be exceeded and the probability is set to 0. Finally, if w_e is less than the lowest tide possible at the Crescent City gauge, ζ_i is always exceeded and the probability is set to 1.

Now, suppose for the moment that the tsunami of Figure 20 consisted of only one wave with a very narrow width, say a spike even. If the tide level at Crescent City at the time this

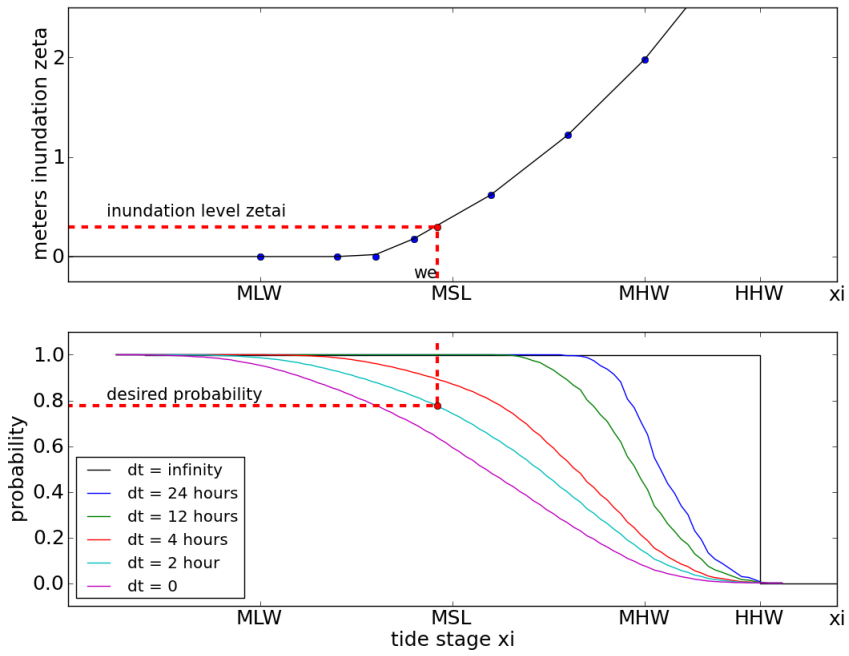

Figure 20: Finding $\xi = w_e$ and $P(\xi > w_e \,|\, \mathrm{dt} = 2)$

wave strikes exceeds w_e, then we say $P(\zeta > \zeta_i) = 1$ because both the tsunami wave and the Crescent City tide support this level of inundation. However, we don't know exactly when the tsunami will strike in the tidal cycle and the level might not exceed w_e. This aleatory uncertainty has been quantified in the cumulative probability distribution function in Figure 19 that gives the probability of exceedance of w_e at any particular instance of time. We refer to this time interval as $\mathrm{dt} = 0$, and say that

$$P(\zeta > \zeta_i \,|\, E_{jk}) = P(\xi > w_e \,|\, \mathrm{dt} = 0). \tag{4}$$

The cumulative probability from Figure 19 is also shown as the curve labelled (dt=0) in the bottom plot in Figure 20. This graph shows how we would extract the desired probability by looking up w_e in the cumulative distribution table (when dt=0 we would drop the dotted vertical line to the bottom graph and then construct another dotted horizontal line to read off the desired probability). This is very convenient, since the question about $P(\zeta > \zeta_i \,|\, E_{jk})$ is changed to a simpler question about the tide levels at Crescent City and the *same* cumulative distribution table can be used for every grid location in Crescent City (only w_e varies across the grid locations).

Next, suppose the tsunami represented in Figure 20 still consists of one wave, but a much wider one (say 15 minutes wide). It is convenient to think of a square wave with constant amplitude over this 15 minute interval. We still can find the constant GeoClaw tide level, w_e, that we need to exceed so that ζ will exceed ζ_i. The issue, though, is that the tide level at Crescent City will not remain constant during a 15 minute interval, although it changes

by at most .18 meters. Do we need the Crescent City tide level ξ to exceed w_e during the entire 15 minutes to report exceedance of ζ_i? Would the same exceedance occur if $\xi > w_e$ for only 7.5 minutes while this square wave were passing into Crescent City. Taking this to the limit, would we still exceed ζ_i if $\xi > w_e$ at only one point in the 15 minute interval when the wave were coming into Crescent City? We don't know the answers to these questions, but choose to err on the side that would give the biggest probability. We will say exceedance of ζ_i occurs if the maximum value, $\hat{\xi}$, of ξ during the 15 minute (.25 hr) interval exceeds w_e, and denote the probability of any 15 minute interval as having a maximum value exceeding w_e as $P(\xi > w_e \,|\, \mathrm{dt} = .25)$. Then, we have

$$P(\zeta > \zeta_i \,|\, E_{jk}) = P(\xi > w_e \,|\, \mathrm{dt} = .25)\,. \tag{5}$$

We can of course consider the one-wave scenerio with waves wider than .25 hours since our experience shows that the wave width typically lasts between 5 and 45 minutes. The procedure is the same, and the requirement is that we are able to create a cumulative distribution table with columns corresponding to the size of dt, and rows corresponding to valid values of w_e. The bottom graph in Figure 20 illustrates several graphs of the columns of such a table, with one graph per column. The limiting case is considering an infinite dt which would correspond to choosing the probability to be 1 if the value of w_e is smaller than the largest tide level seen at Crescent City Gauge No. 9419750 and 0 otherwise.

The cumulative distribution corresponding to a finite dt is gotten as follows. We simply take a dt-window of time and slide it one minute at a time across a year's worth of Gauge 9419750 data. Each time the dt-slider window stops, we find the maximum tide level within the window. We increment a counter in the first bin whose left edge is exceeded by this maximum (to create a histogram) and also in all lower bins (to create a cumulative histogram). Dividing the cumulative histogram by the number of times the dt-slider window stops gives us the cumulative distribution function.

Tsunamis, however, consist of multiple waves of varying amplitudes and widths, and may have the biggest amplitudes spaced apart by hours where nothing capable of changing the maximum exceedance ζ value at a grid location is happening. Multiple waves of nearly or equal magnitude should increase the probability of exceedance of ζ_i since the time frame where w_e could be exceeded increases. Even waves with lesser magnitude than the largest one could produce exceedance of ζ_i if they came into Crescent City at a sufficiently higher tide level than w_e.

Applying the dt-Method to these cases means finding a reasonable way to choose dt. We have the possibility in GeoClaw to record the time history for the tsunami wave (or its effect) at any computational location. Of course, doing this everywhere is prohibitive, but to assist this study, we place GeoClaw Gauge 101 at a location in the water near the Crescent City Gauge 9419750, and GeoClaw Gauge 105 at a point that usually inundates (near the river, but on land). We also have Gauge 33 near the shelf in deeper water, and GeoClaw Gauges 102, 103, and 104 on land. We record what we call the GeoClaw tsunami at Gauge 101, and its biggest effect at the land gauges. Examination of these gauges gives the time intervals and widths of the waves responsible for inundation. The width of the responsible wave of biggest amplitude certainly gives a minimum value for the *contiguous* dt interval, and we

increase dt based on nearby potentially responsible waves.

This method works remarkably well compared to the Pattern-Method described below. For each tsunami, we produced a graph like that in Figure 21 to find the value of dt that would give results close to those of the Pattern method. These values are our recommended dt values for the tsunamis in Table 1. For the two Kamchatka events we recommend KmSZe01 (dt=1) and KmSZe02 (dt=3). For the three Kuril events, we recommend KrSZe01 (dt=2), KrSZe02 (dt=3), and KrSZe03 (dt=4). For the Alaska events, we recommend dt=1 with the exception of AASZe02 (dt=2). The value dt=1 should be used for the Chilean event SChSZ01, the Tohoku event TOHe01, and the Cascadia Bandon CSZBe01r13 and CSZBe01r14 realizations. The value dt=0 should be used for the remaining Cascadia Bandon realizations, CSZBe01r01-CSZBe01r12 and CSZBe01r15. We suspect that choosing dt beyond 4 will give overestimates of the probability as this points to a 4 hour *contiguous* interval.

8.3 The Pattern-Method

This approach grew from the desire to automate the choice of dt in the dt-Method. Instead of achieving this automation of the dt-Method, we developed an even better method that is tailored to each realization's GeoClaw tsunami as seen at GeoClaw Gauge 101. The Pattern-Method uses the relative heights of the wave amplitudes seen at Gauge 101, their widths, and the times they occurred, (with the first wave starting at time 0), to first create a cumulative probability distribution (a table with one column) associated with this particular wave pattern. This is extra work, but the difference is that a fixed dt will not have to be chosen. Instead, the entire pattern will be taken into account to calculate the distribution. Our experience shows that for some tsunamis this new cumulative distribution when compared to the columns of the dt-Method's cumulative distribution gives probabilities similar to a fixed dt (AASZe03 and AASZe08 events), while for other tsunamis the probabilities are consistent with a varying dt (AASZe02 and KrSZe03). To illustrate these findings, we show the pattern cumulative distribution for the AASZe02 event as a dotted line on the same graph as that for the dt-Method with varying dt.

Suppose Gauge 101 has K waves. We model wave W_k with a square wave and record the difference of its amplitude from that of the highest wave as Δ_k. We record the starting and terminating times of W_k as the interval $I_k = [S_k, T_k]$. These times are relative to the start of W_1, so we set $S_1 = 0$, and are recorded in minutes since our gauge 9419750 has minute data. The entire length of the pattern is then T_K minutes, the terminating time of the K-th wave.

In Figure 22, we show the GeoClaw tsunami for the AASZe02 event that was recorded at Gauge 101 as the red graph and the pattern shown as the black graph. The first wave arrived at Crescent City 4 hours after the earthquake and nothing significant was seen there after 11 hours. The pattern is well represented by the 7 waves shown. We are overestimating the probability a bit by using square waves, but we don't have to account for tides during times that they can't possibly have any impact. A table showing the values that describe the pattern are given in Table 3. We note that the first wave began at 263 minutes after the earthquake and the amplitude of the largest wave W_7 was about 1.7 meters. The black

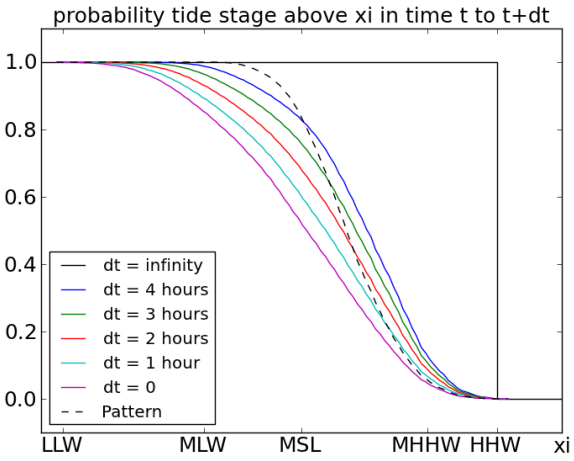

Figure 21: AASZe02: Pattern-Method to dt-Method Cumulative Distribution Comparison

horizontal line starts at .2 meters since the GeoClaw run was done at MHHW which is .2 meters above MHW, the zero level.

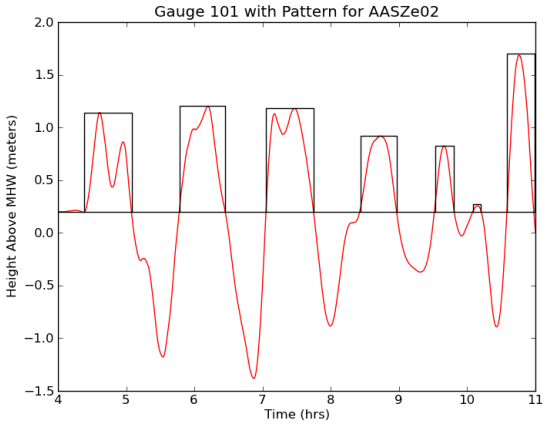

Figure 22: Pattern for AASZe02 at Gauge 101

As in the dt-Method, we take the valid values for the tide levels at Crescent City and put them into a fixed number of bins. But now we take our pattern-slider window that has length T_K and slide it one minute at a time across a year's worth of Gauge 9419750 data. Each time the pattern-slider window stops, we do the following:

- Find the maximum tide level, M_k associated with each I_k, $k = 1 \ldots K$.
- Adjust M_k to get $\bar{M}_k$: $\bar{M}_k = M_k - \Delta_k$.
- Compute $M_P = \max_k \bar{M}_k$.

Table 3: **Pattern Values for AASZe02**

Wave	**I=[S, T] (min)**	**Δ (m)**
W_1	[000, 042]	0.561
W_2	[084, 124]	0.498
W_3	[160, 202]	0.517
W_4	[243, 275]	0.782
W_5	[309, 325]	0.876
W_6	[342, 349]	1.450
W_7	[372, 396]	0.000

- Increment a counter in the first bin whose left edge exceeds M_P, the max for the pattern for this window stop, to create a histogram and also increment in all lower bins to create the cumulative histogram.

Dividing the cumulative histogram by the number of times the pattern-slider window stops gives the cumulative distribution function for the probability of exceeding each valid tide level by a tsunami of this pattern. A table is saved that records the cumulative probabilities for all valid tide levels at the Crescent City gauge 9419750.

After the pattern cumulative distribution is found, the method proceeds exactly as the dt-Method. We use the multiple GeoClaw simulations to find the minimum *constant* tide level $\xi = w_e$ that could be used with GeoClaw to produce inundation height $\zeta = \zeta_i$. If we would make a GeoClaw simulation with tide level w_e (we don't do this), the thinking is that the resulting tsunami pattern at GeoClaw gauge 101 would be the same, with the relative amplitudes the same as using any other tide level. This is because gauge 101 is in the water and records the tsunami as it comes into Crescent City as opposed to being located at a land point that only sees the effect of the tsunami after nonlinear effects have been incorporated.

So, we need to find the probability that the Crescent City tide is sufficient for the tsunami pattern to exceed ζ_i by looking up w_e in our pattern cumulative distribution. We denote the probability that ξ exceeds w_e in the sense of the pattern as $P(\xi > w_e \,|\, \text{pattern})$ with the meaning

$$P(\xi > w_e \,|\, \text{pattern}) = P(\xi > w_e + \Delta_k \,\text{somewhere in}\, I_k \,\text{for some}\, k)\,. \tag{6}$$

Then, we have

$$P(\zeta > \zeta_i \,|\, E_{jk}) = P(\xi > w_e \,|\, \text{pattern})\,. \tag{7}$$

Advantages over the dt-Method

- By adjusting the M_k, we permit the possibility that a wave with amplitude Δ_k less than the maximum one seen at GeoClaw gauge 101 could also cause an inundation of maximum ζ or higher if it occurred at a time where the tide level was at least Δ_k higher than that required of the maximum amplitude gauge 101 wave.

- By looking in each interval I_k, we take into account the actual width of each wave.
- We can ignore what the tide is doing when nothing is happening, and don't have to have a large dt to cover all the action. We only examine the tide during each amplitude, not between amplitudes. This allows a more accurate representation of tsunamis that have a longer duration.
- Only gauge 101 needs to be examined.
- The procedure is automatic. Examining gauge 101 and running the code to generate the cumulative distribution is much faster than examining multiple gauges to make an informed decision about the choice of dt.

Possible limitations

The Pattern-Method requires the simulation code to have GeoClaw's capability of a computational gauge. The dt-Method benefits from examining the gauges to determine dt, but if none were present, the recommended choice would be to use dt=1 for all realizations.

Validation of the Pattern Method

The method of Mofjeld, et.al [26] assumed a proxy tsumami of a given amplitude, a 20 minute period, and a two-day e-folding decay time that lasted 5 days to create a probability density function and related distribution for exceedance of a specified ζ level. These formulas were converted to distributions of the tide stage, and compared to what the Pattern Method would give *if* the tsunami seen at Gauge 101 were this proxy tsunami. We then ran the Pattern Method on this proxy tsunami (with amplitude taken as that of the biggest wave seen at Gauge 101 for AASZe03) and created the Pattern Method cumulative distribution. The two when plotted are almost identical with values differing mostly less than 1% as seen in Figure 23 as the green and dashed red graphs.

This explains any differences generated by the Mofjeld method and the Pattern Method at the Gauge 101 for any real tsunami is not due to our methodology, but to the fact that the real tsunami is not well approximated by the proxy one. The Pattern Method can capture the differences of each specific tsunami as seen in Figure 23 by the differences between the black graph and the green (or dashed red) ones.

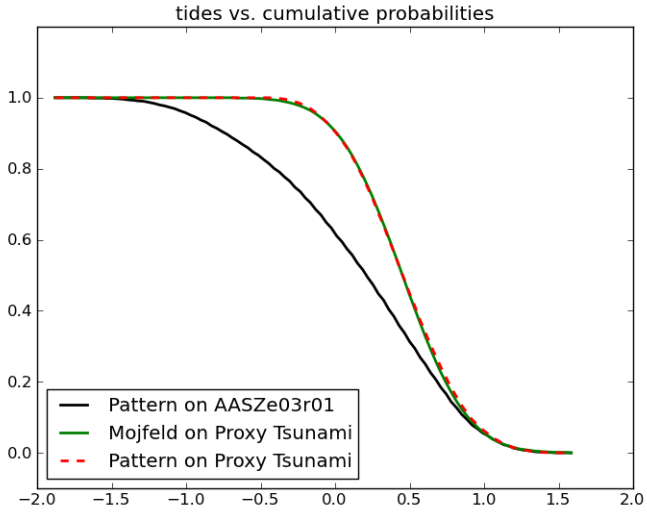

Figure 23: Pattern Method Validation

9 Regulatory and non-regulatory products

9.1 Regulatory products – ζ-contour maps

The *regulatory products* required by FEMA are 100-year and 500-year hazard maps, which are shown in Section 3. In this section we discuss some other ways to visualize probabilistic results that may be useful to consider.

9.2 Non-regulatory products of potential value –p-contour maps

We believe that viewing only 100-year and 500-year maps may be misleading and that more information is available than is displayed in this format. In this section we point out the limitations and suggest some other products that may be useful to consider.

Our primary concerns with the regulatory products are:

- The lines showing maximum inundation at the probability levels $p = 0.01$ and $p = 0.002$ can be highly sensitive to changes in the input (such as the recurrence time of some events) and also to the choice of these two particular p values.

- There is the possibility of much greater inundation distances than shown on either of the above maps, if it has probability less than 0.002. It may be useful for emergency managers to know about the potential for greater flooding than is shown on these maps, even if the probability is less than the somewhat arbitrary value of 0.002.

To give an illustration of these concerns, consider a simplified hypothetical case in which there is only one possible earthquake in the study — one particular CSZ Mw 9.1 event realization and suppose it has a recurrence time of 499 years. Then our methodology would

result in the 500-year map shown on the left in Figure 24, with a large region of possible inundation.

Now consider the same situation but suppose the recurrence time for this one event is 501 years rather than 499 years. Then the 500-year map on the right in Figure 24 results. This map shows no inundation at all, since at every (x, y) point the probability of $\zeta > 0$ is either 0 or $1 - \exp(-1/501) \approx 0.001994 < 0.002$.

Similarly, if we left the recurrence time at 499 years but plotted the inundation map for $p = 0.00201$ rather than for $p = 0.002$, the hazard map would again change to that on the right in Figure 24 since $1 - \exp(-1/499) \approx 0.002002 < 0.00201$.

The above example illustrates that looking at contours of ζ for particular fixed values of p, such as 0.01 and 0.002, can fail to show significantly greater potential inundation that is only slightly less probable.

The ζ-contour maps for fixed p are useful, since they give not only a view of the region inundated with these probabilities but also the depth of inundation at each point that can be expected with these annual probabilities. However, we believe that in addition to these maps it would be useful to also view maps that show *contours of probability* for which a particular inundation depth $\bar{\zeta}$ is exceeded. These are also easily generated from the hazard curves that are generated in our PTHA methodology. At each grid point (x, y) in the region of interest, the hazard curves show directly the probability of exceeding $\bar{\zeta}$. Evaluating this at each grid point allows generating a contour map of p for this $\bar{\zeta}$.

Note in particular that choosing exceedance value $\bar{\zeta} = 0$ will then show the contours of probability for any inundation (i.e., $\zeta > 0$) at each point. In particular the $p = 0.01$ contour of this map will be the limits of the region that experiences any flooding with probability 0.01 and should agree with the limits of the inundation region shown on the 100-year hazard map.

Figure 25 shows contours of p for the exceedance value $\bar{\zeta} = 0$ for the simple examples used above to illustrate sensitivity. (Actually these show a color map in which color indicates probability, and the boundary between colors are contour lines.) Again the plot on the left is what is obtained if we assume a recurrence time of 499 years for the one event considered, and the plot on the right is if we assume a recurrence time of 501 years. The two plots now look very similar, though the color is slightly different indicating a slight change in the probabilities. However the $p = 0.002$ contour line is near the outer limits of the colored region in the left plot while in the right plot there is no region with $p \geq 0.002$.

It may also be useful to look at contour plots of p for different choices of exceedance level $\bar{\zeta}$. For example, choosing $\bar{\zeta} = 1$m would show probabilities of exceeding 1 meter of inundation at each point. There may be particular depths that are considered hazardous and more meaningful to consider than $\bar{\zeta} = 0$. Some examples are given in the next section.

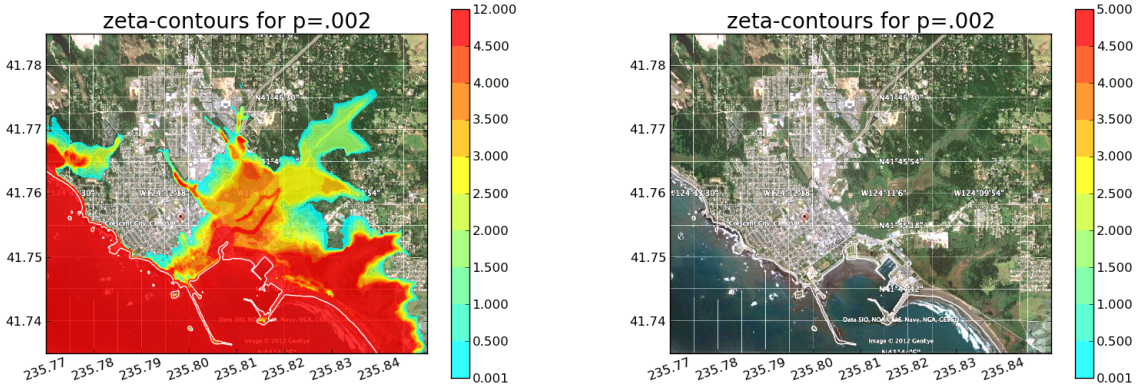

Figure 24: ζ-contours for p=.002 when only one sample event is considered. Left: assuming recurrence=499 years. Right: assuming recurrence=501 years.

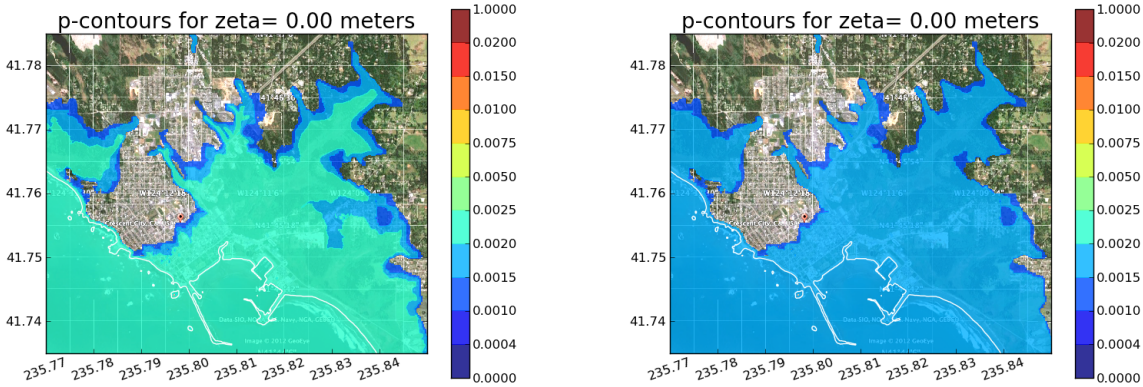

Figure 25: p-contours for $\zeta = 0$ m, when only one sample event is considered. Left: assuming recurrence=499 years. Right: assuming recurrence=501 years.

9.3 Sample p-contour maps

Figure 26 shows p-contours for exceedance level $\bar{\zeta} = 0$ based on the same set of events used for the regulatory products shown in Section 3. Note that the $p = 0.01$ contour of Figure 26 agrees with the extent of inundation shown in Figure 3, and the $p = 0.002$ contour of Figure 26 agrees with the extent of inundation shown in Figure 4. Black lines in the figures mark the $p = .01$ and $p = .002$ contours and the white line is the shore line associated with $B = 0$. Figure 27 shows p-contours for different values of exceedance $\bar{\zeta}$.

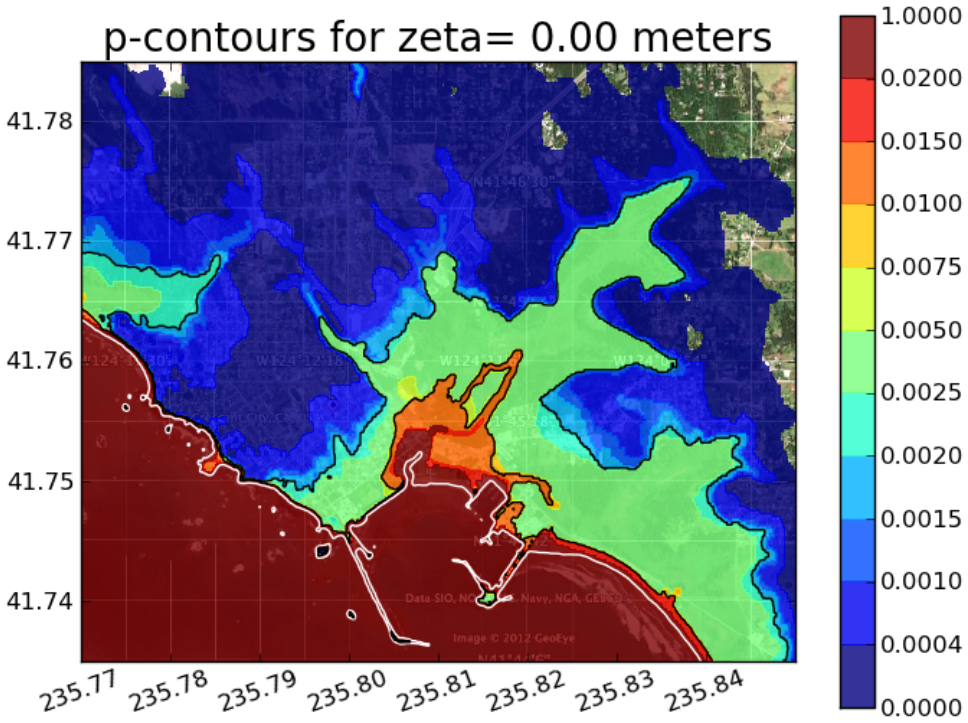

Figure 26: p-contours, ζ=0.0 meters, with the study sources of Table 1. This includes the Bandon study sources for CSZ with $T_M = 332$ years and a representative Japan source with $T_M = 103$ years.

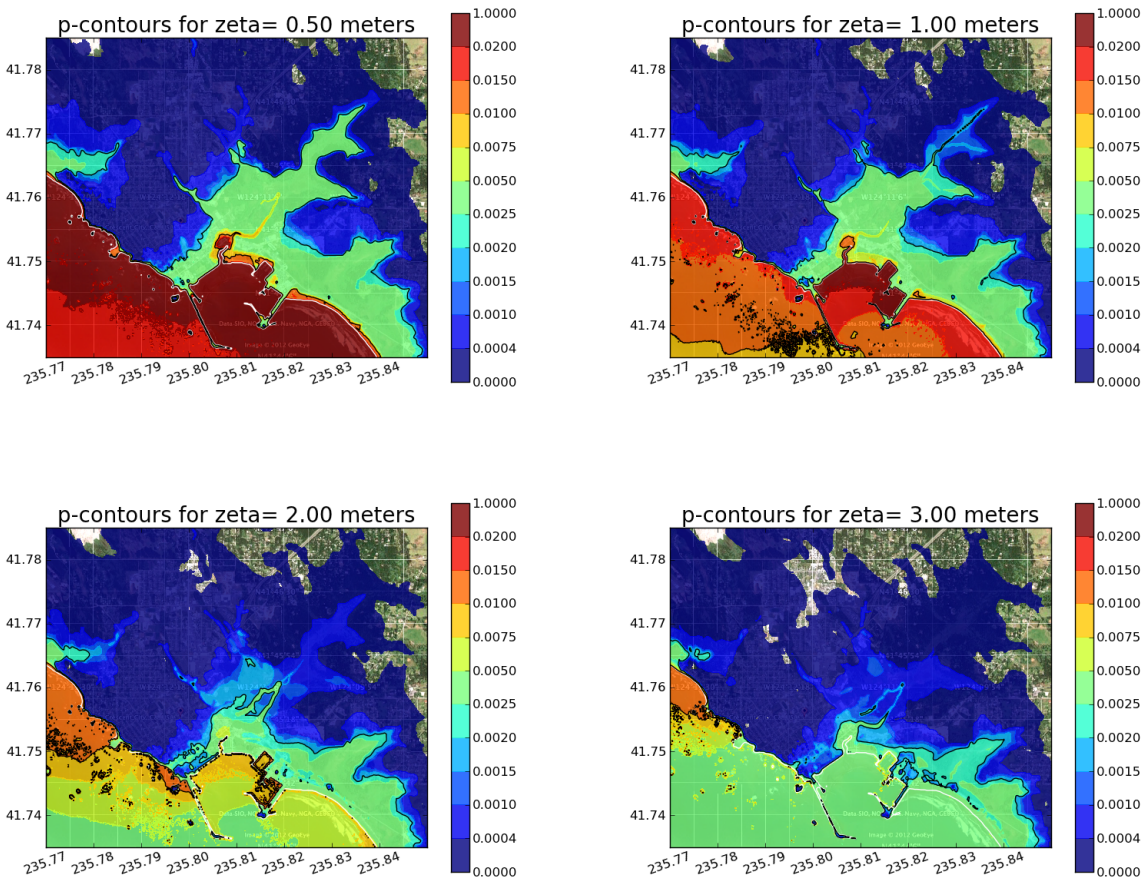

Figure 27: p-contours for other exceedance levels.

9.4 Transects

In addition to contour plots, it is also useful to view one-dimensional transects of the results. Figure 28 and Figure 29 show two examples of such plots. In each case there is a plot of cross sections of the 100-year and 500-year inundations (ζ at fixed probabilities $p = 0.01$ and $p = 0.002$), corresponding to Figure 3 and Figure 4, and also cross sections of the probability of exceeding various ζ values corresponding to Figure 26 and Figure 27.

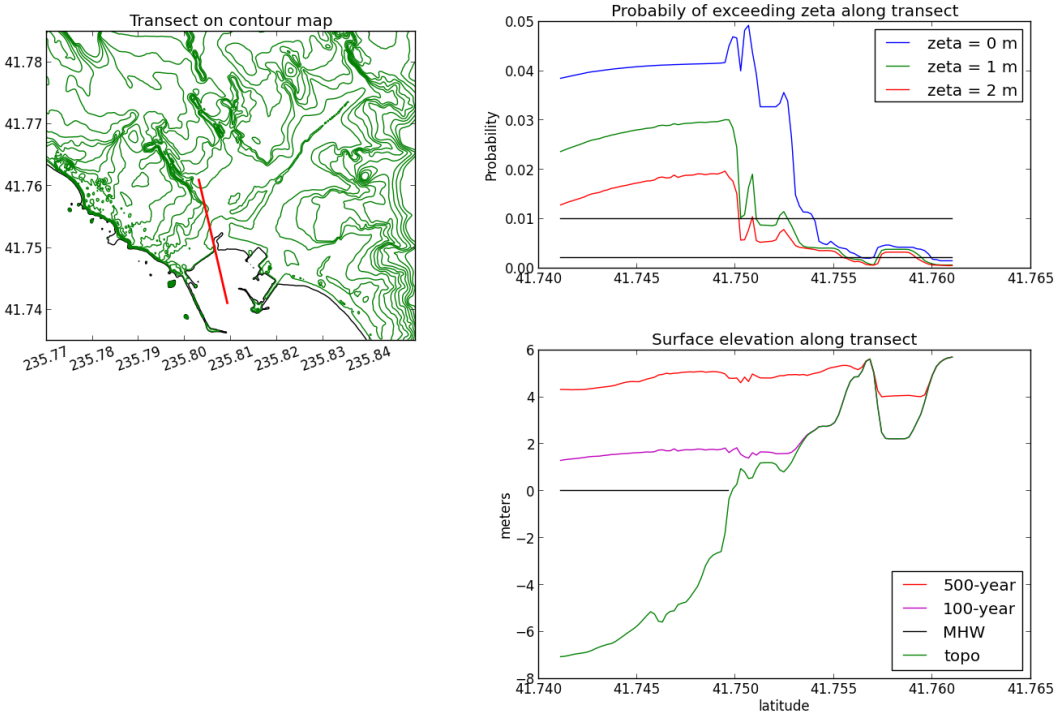

Figure 28: Sample transect plots.

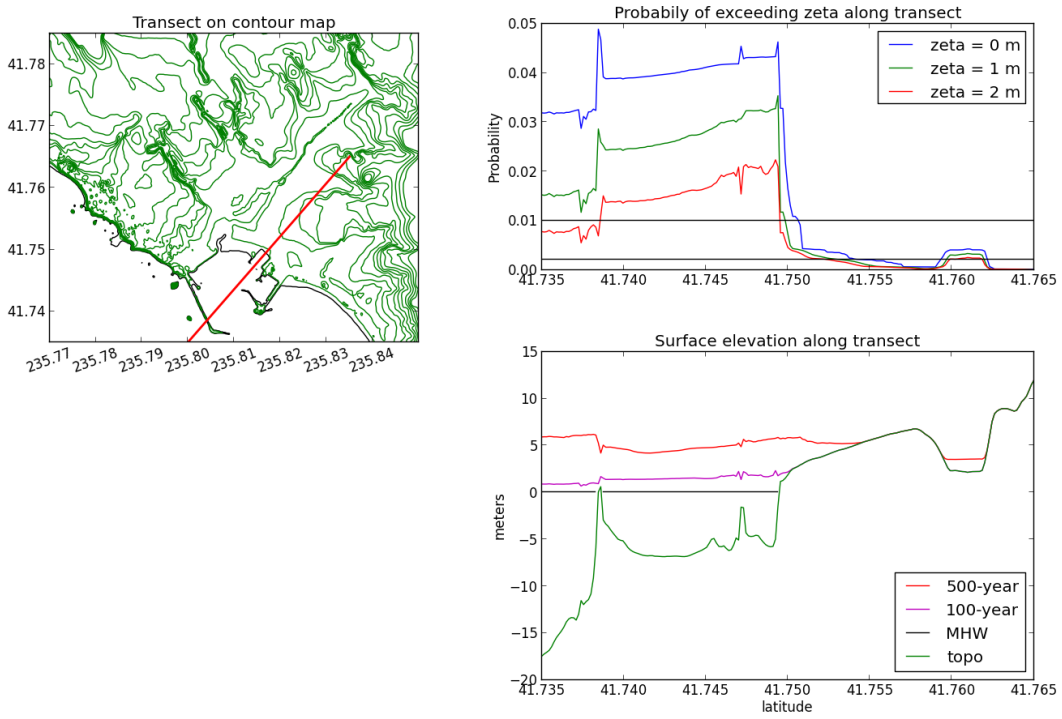

Figure 29: Sample transect plots.

9.5 $T_M = 332$ vs. $T_M = 525$ Results

The regulatory products shown in Figures 3 and 4, the p-contours in Figure 26 and Figure 27, and the Transects in Figure 28 and Figure 29 used the sources in Table 1 and assumed the recurrence time of the Cascadia source was 332 years. In this section, we compare some of these products with those that would be obtained if 525 years were used instead for the recurrence time of the Cascadia source. Figure 30 shows the 100 and 500 year flood comparisons. Figure 31 compares the p-contours for $\zeta = 0$ and $\zeta = 1$ and Figure 32 compares the p-contours for $\zeta = 2$ and $\zeta = 3$.

Indeed the Cascadia source produces the largest inundation of Crescent City from the sources in Table 1 whenever it occurs. However, the recurrence rate that should be used for this earthquake (for which we use the 15 Bandon realizations) is still subject to debate (see Section 7.6.1). We ran the Geoclaw simulations using both 332 years and 525 years as the recurrence rate. It is interesting to note that when combined with the results from the other sources in Table 1, the probabilistic analysis shows the 100yr and 500yr floods to be quite similar, see Figure 30. This is in complete contrast to the ζ-contours for $p = .002$ gotten from using only the Cascadia sources from Table 1, see Figure 33. This points out that the extent of the 500-year flood lines in the right plot in Figure 30 is due to Alaskan as well as Cascadia sources. This is seen from the p-contour ($\zeta = 0$) plots in Figure 35.

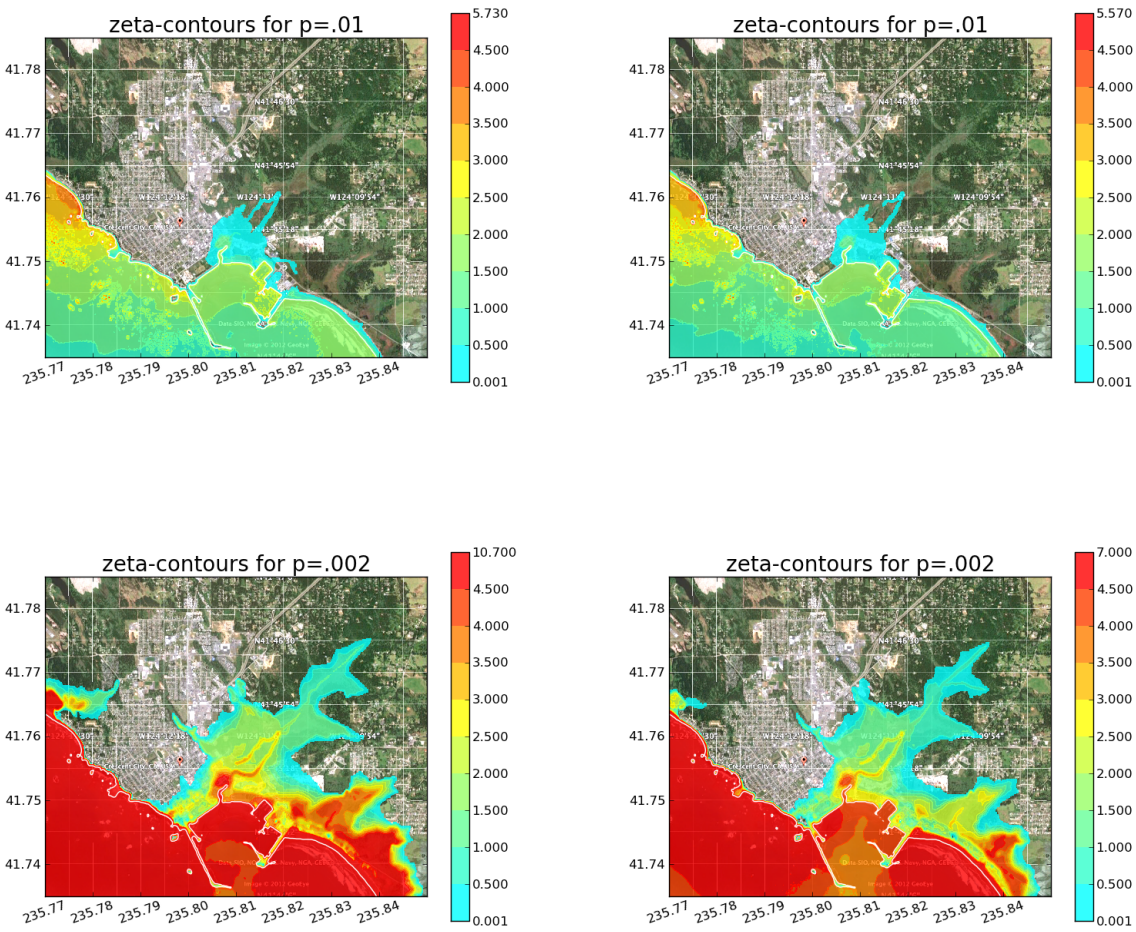

Figure 30: ζ-contours for Table 1 sources for p=.01 (Top) and p=.002 (Bottom), with $T_M = 332$ (left) and $T_M = 525$ (right)

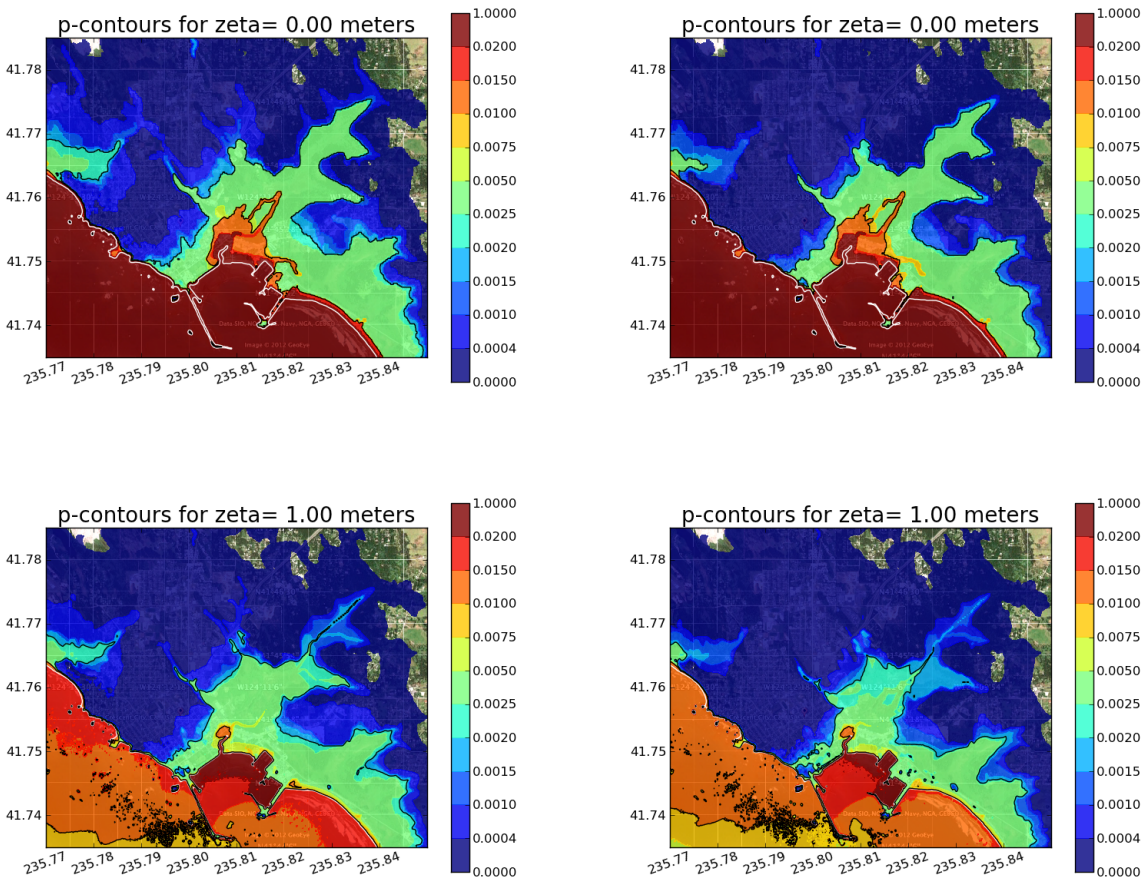

Figure 31: p-contours for Table 1 sources. Top: $\zeta = 0$, for $T_M = 332$ (left) and $T_M = 525$ (right). Bottom: $\zeta = 1$, for $T_M = 332$ (left) and $T_M = 525$ (right)

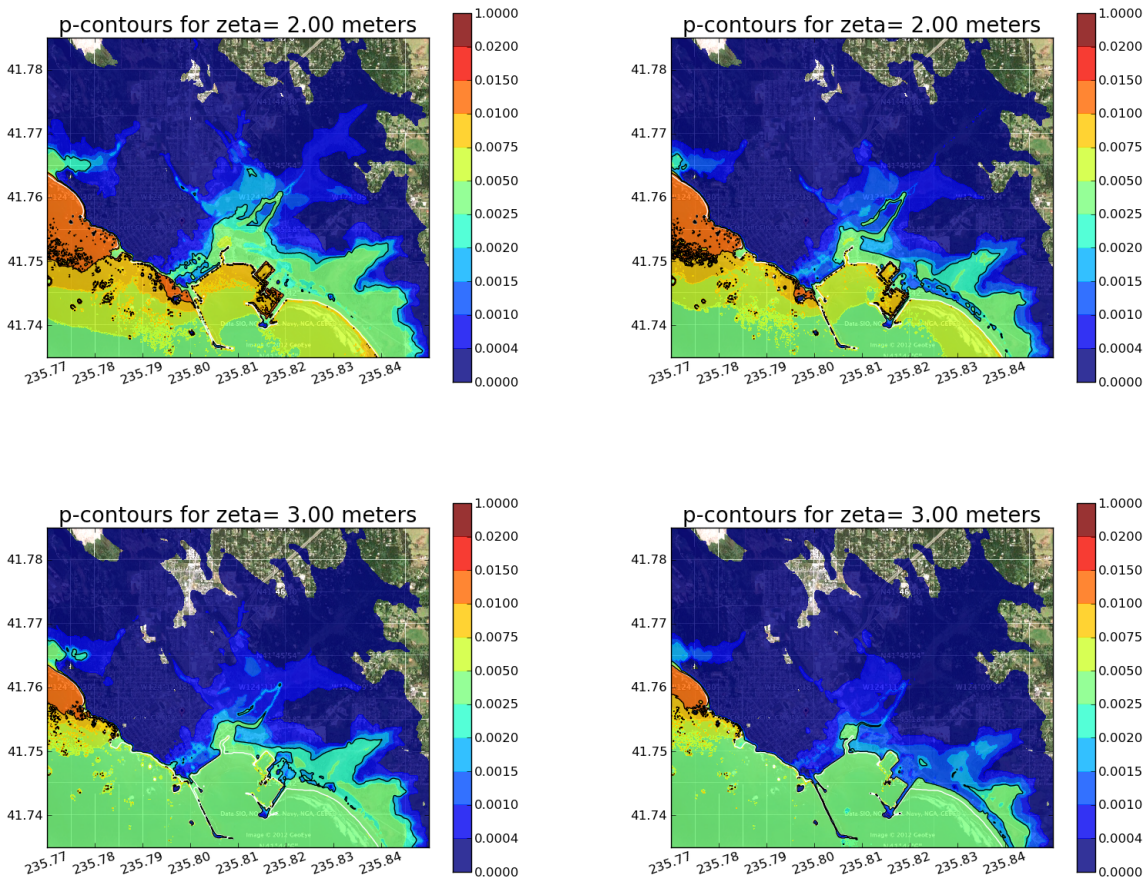

Figure 32: p-contours for Table 1 sources. Top: $\zeta = 2$, for $T_M = 332$ (left) and $T_M = 525$ (right). Bottom: $\zeta = 3$, for $T_M = 332$ (left) and $T_M = 525$ (right)

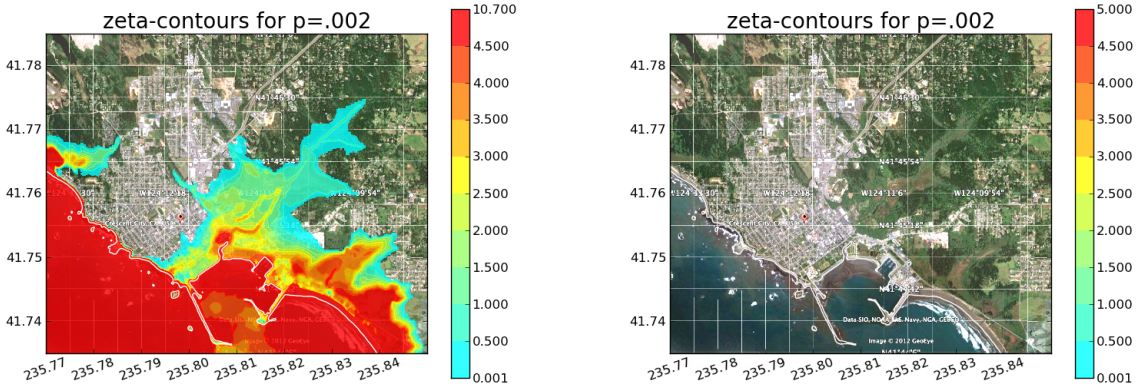

Figure 33: ζ-contours for just Cascadia sources for p=.002. Left: $T_M = 332$, and Right: $T_M = 525$

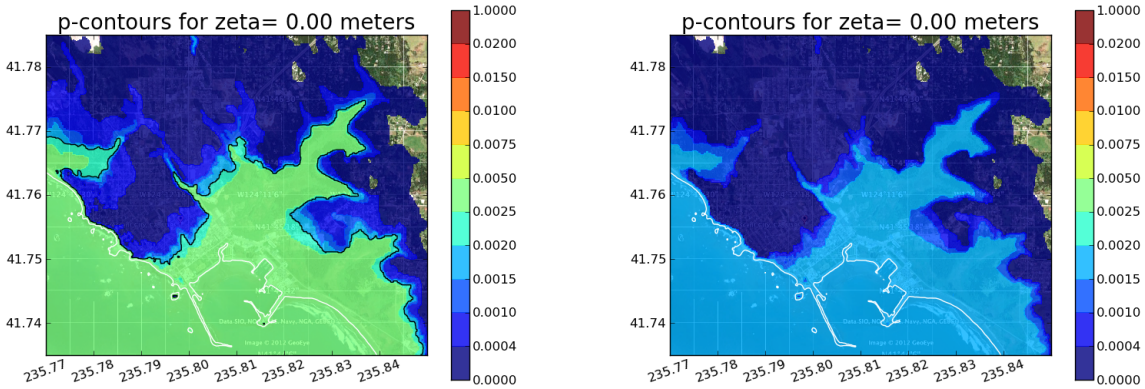

Figure 34: p-contours for $\zeta = 0$. Left: Only Cascadia $T_M = 332$, Right: Only Cascadia $T_M = 525$

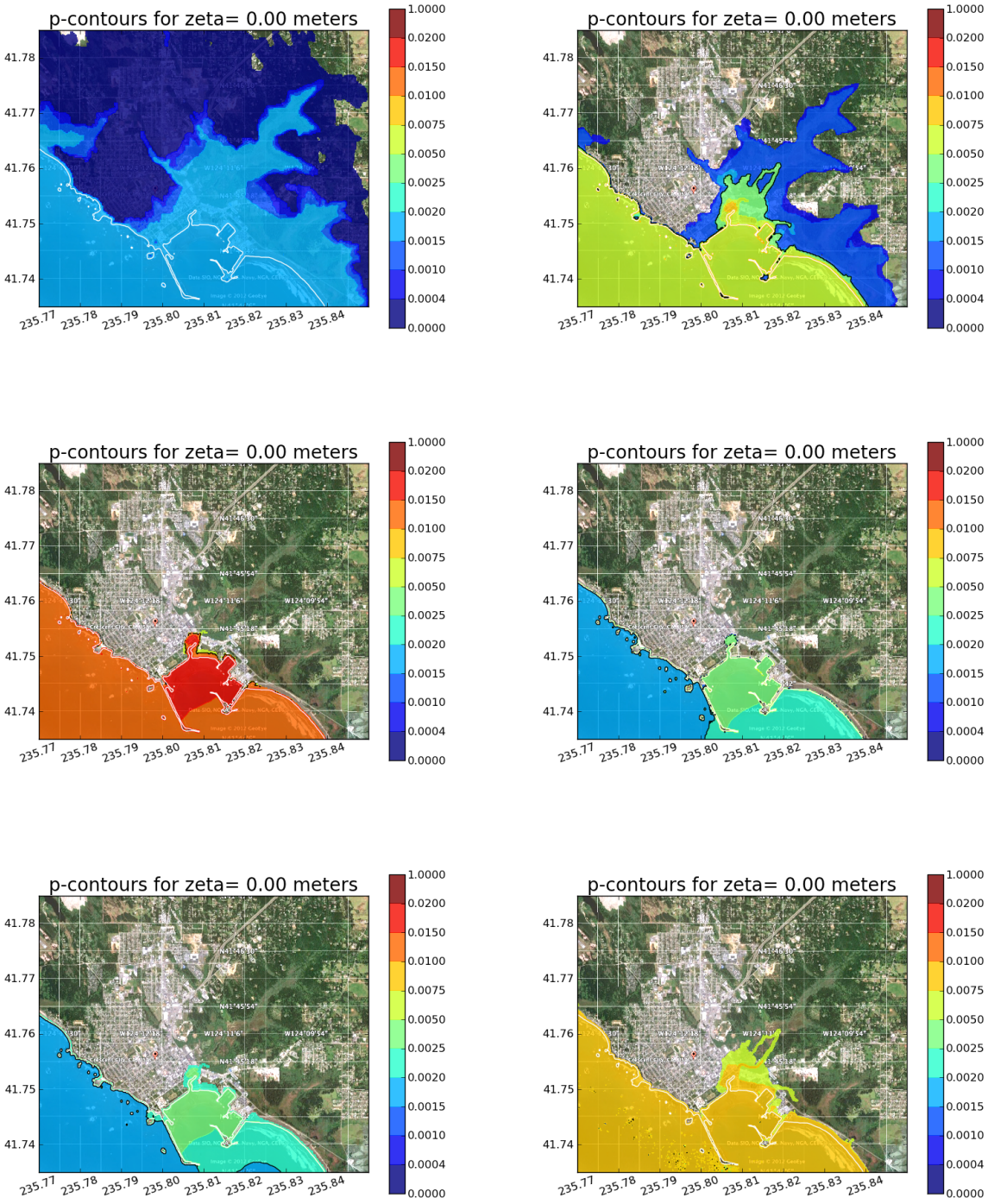

Figure 35: p-contours for $\zeta = 0$. Top left: Only Cascadia $T_M = 525$, Top right: All AASZ Only, Middle left: All KmSZ Only, Middle right: All KrSZ Only, Bottom left: SChSZe01 Only, Bottom right: TOHe01 Only

10 Conclusions

The primary regulatory products resulting from this work are the 100-year and 500-year flood maps based on our probabilistic modeling. These are presented in Section 3. This modeling required the choice of a set of earthquake sources (seafloor deformation) along with the recurrence time for such an earthquake. A set of appropriate sources was developed in Section 7. The GeoClaw software described in Section 5 was used to perform a tsunami propagation and inundation simulation at three different static tide levels for each source. Tidal uncertainty was incorporated using a new "pattern method" technique discussed in Section 8. From all of these simulation results, a hazard curve can be computed at each grid point on the spatial grid covering Crescent City, as described briefly in Section 3.3 and more fully in Appendices A and B. From this set of hazard curves, the regulatory maps can be easily created by interpolating to find the inundation depth ζ for the probabilities $p = 0.01$ and $p = 0.002$.

It is also possible to create other non-regulatory products, such as contour maps of probability for a fixed inundation depth or plots of any of these quantities along a one-dimensional transect. In Section 9.2 we discuss some of the limitations of the regulatory products and the possible complementary use of other products.

10.1 Limitations

There are many limitations of the current study and the results should be viewed in this light. Some of the things that require further study are:

- Earthquake sources. We believe this is the largest source of error in the probabilistic results, since the epistemic uncertainty of determining the proper probability distributions of possible events has not been fully addressed.

- Our attempts at modeling tidal uncertainty are not perfect. Moreover we do not model the currents that are generated by the tide rising and falling. A tsunami wave arriving on top of an incoming tide could potentially inundate further than the same amplitude wave moving against the tidal current, even if the tide stage is the same. Modeling this is beyond the scope of current tsunami models.

- Instantaneous uplift is assumed. Some tsunami models include dynamic rupture and even the effect of finite acoustic speed in water, which results in a somewhat different displacement of the sea surface than the seafloor. Based on past validation of the code (Section 5.3 through 6.2), we do not think this will make a significant difference, particularly since the sea floor deformations are meant to be random samples rather than models of particular events.

- We have used the constant Manning coefficient $n = 0.025$ everywhere. It would be better to use a variable friction coefficient that takes into account the variable surface roughness. We have followed standard practice with use of this constant value.

- The topography is "bare earth" and does not include structures. This fact, together with the use of a relatively small Manning coefficient, means the inundation distances computed may be greater than they should be.
- The depth-averaged shallow water equations are less accurate in the inundation region, where three-dimensional effects can be important, than offshore. Moreover, the water will be mixed with debris onshore and become more of a debris flow rather than pure water, which might be better modeled by other equations.

10.2 Future directions

Phase II of this study is now underway, a probabilistic study of tsunami currents and momentum flux.

Improvement of the GeoClaw software for modeling individual events is continuing. Features such as spatially varying Manning friction coefficients could allow more accurate simulations.

Further improvements in probabilistic results might be accomplished if it were possible to better describe the probability distribution of potential events. This is primarily a geophysics problem, but we have started to explore some of the mathematical techniques that could be useful in describing and efficiently sampling from a given probability density. Because it may require many stochastic parameters to describe a random slip pattern over the fault geometry, the resulting stochastic space is very high dimensional. One approach to describing the slip is by using a Karhunen-Loève expansion in the framework of random spatial methodologies such as Mai and Beroza [24], in which the spatial pattern is written as a linear combination of modes that are taken to be the eigenvectors of a desired covariance matrix. The coefficients are then independent random variables. We put considerable effort into this as a possible way to generate new CSZ realizations. We feel it is a promising approach for future work, but were not able to determine the necessary parameters sufficiently well to make use of this in the present study.

Once a high-dimensional probability density is determined, there are various techniques that may be useful to efficiently sample such a distribution and compute the desired probabilities of inundation. Dimension reduction techniques, importance sampling, multi-level Monte-Carlo, and stochastic collocation are some ideas from the Uncertainty Quantification (UQ) literature that we have started to pursue.

References

[1] K. Abe. Size of great earthquake of 1837-1974 inferred from tsunami data. *J. Geophys. Res.*, 84:1561–1568, 1979.

[2] C. Amante and B. W. Eakins. ETOPO1 1 Arc-Minute Global Relief Model: Procedures, Data Sources and Analysis. NOAA Technical Memorandum NESDIS NGDC-24, U.S. Dept. of Commerce, Boulder, CO, 2009.

[3] D. Arcas and B. Uslu. A tsunami forecast model for Crescent City, California. PMEL Tsunami Forecast Series: Vol. 2, NOAA OAR Special Report (April 8), 2010.

[4] M. E. M. Arcos and R. J. LeVeque. Velocity measurements near Hawaii compared to model simulations of the 11 March 2011 Tohoku tsunami. *J. Geophys. Res.*, submitted.

[5] S. E. Barrientos and S.N. Ward. The 1960 Chile earthquake: Inversion for slip distribution from surface deformation. *Geophysical Journal International*, 104:589–598, 1990.

[6] M. J. Berger, D. L. George, R. J. LeVeque, and K. T. Mandli. The geoclaw software for depth-averaged flows with adaptive refinement. Preprint and simulations: `www.clawpack.org/links/papers/awr10`, 2010.

[7] J. L. Blair, P. A. McCrory, and D. H. Oppenheimer. A geo-referenced 3d model of the Juan de Fuca Slab and associated seismicity. `http://pubs.usgs.gov/ds/633/`, 2012.

[8] I. L. Cifuentes. The 1960 Chilean earthquakes. *J. Geophys. Res.*, 94:665–680, 1989.

[9] I.L. Cifuentes and P.G. Silver. Low-frequency source characteristics of the great 1960 Chilean earthquake. *J. Geophys. Res.*, 94:643–663, 1989.

[10] D. L. George. *Finite Volume Methods and Adaptive Refinement for Tsunami Propagation and Inundation*. PhD thesis, University of Washington, 2006.

[11] F. González, R. J. LeVeque, J. Varkovitzky, P. Chamberlain, B. Hirai, and D. L. George. GeoClaw Results for the NTHMP Tsunami Benchmark Problems. `http://depts.washington.edu/clawpack/links/nthmp-benchmarks/geoclaw-results.pdf`, 2011.

[12] F. I. González, E L Geist, B. Jaffe, U Kanoglu, et al. Probabilistic tsunami hazard assessment at Seaside, Oregon, for near-and far-field seismic sources. *J. Geophys. Res.*, 114:C11023, Jan 2009.

[13] P.R. Grothe, L.A. Taylor, B.W. Eakins, K.S. Carignan, R.J. Caldwell, E. Lim, and D.Z. Friday. Digital elevation models of Crescent City, California: Procedures, data sources and analysis. NOAA Technical Memorandum NESDIS NGDC-51, U.S. Dept. of Commerce, Boulder, CO, 2011.

[14] TPSWG (Tsunami Pilot Study Working Group). Seaside Oregon Tsunami Pilot Study-modernization of FEMA flood hazard maps. NOAA OAR Special Rep., NOAA/OAR/PMEL, Seattle, WA, 94 pp. +7 appendices, 2006.

[15] Japan Earthquake Research Center (JERC). Year 2013 calculation reference date (2013) January 1 summary of long-term evaluation of subduction-zone earthquakes. http://www.jishin.go.jp/main/choukihyoka/kaikou.htm with map http://wwwjishin.go.jp/main/p_hyoka02.htm, 2012.

[16] J. M. Johnson and K. Satake. Asperity distribution of the 1952 Great Kamchatka earthquake and its relation to future earthquake potential in Kamchatka. *Pure and Applied Geophysics*, 154:541–553, 1999.

[17] R. J. LeVeque. *Finite Volume Methods for Hyperbolic Problems*. Cambridge University Press, 2002.

[18] R. J. LeVeque and D. L. George. High-resolution finite volume methods for the shallow water equations with bathymetry and dry states. In P. L-F. Liu, H. Yeh, and C. Synolakis, editors, *Advanced Numerical Models for Simulating Tsunami Waves and Runup*, volume 10, pages 43–73, 2007. http://www.amath.washington.edu/ rjl/pubs/catalina04/.

[19] R. J. LeVeque, D. L. George, and M. J. Berger. Tsunami modeling with adaptively refined finite volume methods. *Acta Numerica*, pages 211–289, 2011.

[20] A. T. Linde and P. G. Silver. Elevation changes and the great 1960 Chilean earthquake–support for aseismic slip. *Geophys. Res. Lett.*, 16:1305–1308, 1989.

[21] P. L. F. Liu, Y. S. Cho, S. B. Yoon, and S.N. Seo. 1960 Chilean tsunami propagation and inundation at Hilo, Hawaii. In Y. Tsuchiya, N. Shuto, and Kluwer Academic Publishers, editors, *In Tsunami: Progress in Prediction, Disaster Prevention and Warning*, pages 99–115, 1995.

[22] B. T. MacInnes, A. R. Gusman, R. J. LeVeque, and Y. Tanioka. Comparison of earthquake source models for the 2011 Tohoku-oki event using tsunami simulations and near field observations. submitted, preprint at http://faculty.washington.edu/rjl/pubs/tohoku1/, 2012.

[23] O. Magoon. Structural damage by tsunamis. Proceedings American Society of Civil Engineers , Specialty Conference on Coastal Engineering, Santa Barbara, CA, Chapter 4, Oct., 1965.

[24] P. M. Mai and G. C. Beroza. A spatial random field model to characterize complexity in earthquake slip. *J. Geophys. Res.*, 107:?, 2002.

[25] P. A. McCrory, J. L. Blair, F. Waldhauser, and D. H. Oppenheimer. Juan de Fuca slab geometry and its relation to Wadati-Benioff zone seismicity. *J. Geophys. Res.*, 117:B09306, September 2012.

[26] H.O. Mofjeld, F.I. Gonzáles, V.V. Titov, A.J. Venturato, and J.C. Newman. Effects of tides on maximum tsunami wave heights: Probability distributions. *J. Atmos. Ocean. Technol.*, 24(1):117–123, 2007.

[27] F. Nanayama, K. Satake, R. Furukawa, K. Shimokawa, B.F. Atwater, K. Shigeno, and S. Yamaki. Unusually large earthquakes inferred from tsunami deposits along the Kuril trench. *Nature*, 424:660–663, 2003.

[28] Proceedings and results of the 2011 nthmp model benchmarking workshop. U.S. Department of Commerce/ NOAA/NTHMP; (NOAA Special Report). 436 p., http://nthmp.tsunami.gov/documents/nthmpWorkshopProcMerged.pdf, 2011.

[29] M. D. Petersen, C. H. Cramer, and A. D. Frankel. Simulations of Seismic Hazard for the Pacific Northwest of the United States from Earthquakes Associated with the Cascadia Subduction Zone. *Pure Appl. Geophys.*, 159:2147–2168, 2002.

[30] T. K. Pinegina, J. Bourgeois, L. Bazanova, I. V. Melekestsev, and O.A. Braitseva. A millennial-scale record of Holocene tsunamis on the Kronotskiy Bay coast, Kamchatka, Russia. quaternary research. *Quaternary Research*, 59:36–47, 2003.

[31] F. F. Pollitz, P. A. McCrory, D. Wilson, J. Svarc, C. Puskas, and R. B. Smith. Viscoelastic-cycle model of interseismic deformation in the northwestern United States. *Geophysical Journal International*, 181:665–696, March 2010.

[32] L. J. Ruff and H. Kanamori. The rupture process and asperity distribution of three great earthquakes from long-period diffracted p-waves. *Physics of the Earth and Planetary Interiors*, 31:202–230, 1983.

[33] I. Salgado, A. Eipert, B.F. Atwater, M. Shishikura, and M. Cisternas. Recurrence of giant earthquakes inferred from tsunami sand sheets and subsided soils in southcentral Chile (abstract). Geological Society of America Abstracts with Programs, 2003.

[34] C. H. Scholz. *The mechanics of earthquakes and faulting*. Cambridge University Press, 1990.

[35] G. Shao, X. Li, C. Ji, and T. Maeda. Focal mechanism and slip history of 2011 mw 9.1 off the Pacific coast of Tohoku earthquake, constrained with teleseismic body and surface waves. *Earth Planets Space*, 63:559–564, 2011.

[36] V. V. Titov and F. Gonzales. Implementation and testing of the method of splitting tsunamis (MOST) model. NOAA Tech. Memo. ERL PMEL-112, 1997.

[37] S. N. Ward. Earthquake mechanisms and tsunami generation: The Kuril Islands event of 13 October 1963. *Bulletin of the Seismological Society of America*, 72:759–777, 1982.

[38] R. Wilson, A. Admire, J. Borrero, L. Dengler, M. Legg, P. Lynett, K. Miller, A. Ritchie, K. Sterling, and P. Whitmore. Observations and impacts from the 2010 Chilean and 2011 Japanese tsunamis in California. *Pure and Applied Geophysics*, 2012.

[39] R. Wilson, K. Miller, C. Davenport, T. Nicolini, L. Dengler, A. Admire, and C. Synolakis. Comparison of strong currents and impacts on the California (USA) maritime communities from the 2010 Chile and 2011 Japan Teletsunamis. American Geophysical Union fall meeting 2011, Abstract NH1AA-1342, December 9: 1-1, 2011.

[40] R. C. Witter, Y. Zhang, K. Wang, G. R. Priest, C. Goldfinger, L. L. Stimely, J. T. English, and P. A. Ferro. Simulating tsunami inundation at Bandon, Coos County, Oregon, using hypothetical Cascadia and Alaska earthquake scenarios. Oregon Department of Geology and Mineral Industries Special Paper 43, 2011.

APPENDICES

A Generating hazard curves ignoring tidal variation

A key step in our probabilistic approach to producing hazard maps is the generation of a *hazard curve* at each point on a fine grid covering Crescent City and the surrounding area. The terminology of hazard curves has been used for many years in probabilistic *seismic* hazard assessment (PSHA) and has been adopted in PTHA and used in past studies such as [12]. The hazard curve for inundation at a fixed (x, y) location (longitude and latitude) shows maximum depth of inundation ζ on the horizontal axis and probability of exceeding this value on the vertical axis. This is a cumulative probability function, but the fact that we consider the probability of *exceeding* each value means the probability does not generally approach 1 as $\zeta \to 0$. Instead, the value $P(0; x, y)$ is the probability of having any flooding $(\zeta > 0)$ at this point (x, y).

A sample hazard curve is shown in Figure 36 for the point $(235.80719, 41.75391)$, the location of Gauge 105 in Figure 2. This simple example was created by assuming that the only possible events are the first 3 AASZ characteristic tsunamis discussed in Section 7.1, and using the recurrence times from Table 4. We have also ignored tidal uncertainty to begin with and only consider inundation computed when the simulation is run at MHHW. The incorporation of tidal uncertainty is discussed in the next section.

By examining the synthetic tide gauge records at Gauge 105 for each of the three AASZ sources, the maximum depth of water, $\hat{\zeta}$, at this point can be determined for each scenario, with the maximum depths and annual probability of occurrence as given in Table 4.

AASZe01:	$\hat{\zeta}_1 = 1.9$ m	$p_1 = 1/1313 = 0.000762$
AASZe02:	$\hat{\zeta}_2 = 1.3$ m	$p_2 = 1/750 = 0.00133$
AASZe03:	$\hat{\zeta}_3 = 4.0$ m	$p_3 = 1/750 = 0.00133$

Table 4: Three distinct AASZ events with the depth they inundate at one fixed (x, y) point.

We see from this data that there is 0 probability of exceeding depth $\zeta = 4$, while for any value of ζ between 1.9 and 4, the probability of exceedance is $p_3 = 0.00133$, since only one event AASZe03 inundates to this level.

On the other hand there are two events (AASZe03 and AASZe01) that exceed 1.3 m, and so for any ζ between 1.3 and 1.9 the probability of exceedance must be computed taking into account that either event might occur.

If two events are independent with annual probabilities p_i and p_j then the probability of at least one event happening is

$$p_{ij} = 1 - (1 - p_i)(1 - p_j) = p_i + p_j - p_i p_j \approx p_i + p_j.$$

Hence the probability of event 1 or 3 happening is $p_{13} \approx 0.0021$, and this is the value displayed on the hazard curve for $1.3 < \zeta < 1.9$. Note that if $p_i = 1 - e^{-\mu_i}$ and $p_j = 1 - e^{-\mu_j}$

then $p_{ij} = 1 - e^{-\mu_i} e^{-\mu_j} = 1 - e^{-(\mu_i + \mu_j)}$, so the combined probability can also be computing by adding the Poisson rates $\mu_i = 1/T_i$.

Similarly, for $0 < \zeta < 1.3$ there are three possible events (AASZe03, AASZe01, or AASZe02) that give this level of inundation and so for any ζ in this range the probability of exceedance is $p_{134} = 0.0034$, computed via

$$p_{ijk} = 1 - (1 - p_i)(1 - p_j)(1 - p_k) = p_{ij} + p_k - p_{ij}p_k \approx p_i + p_j + p_k.$$

The latter approximation is valid if all probabilities are much less than 1. Similar formulas hold when more than 3 events are considered.

With only three possible discrete events to consider, the hazard curve is piecewise constant with jump discontinuities at the values $\zeta = \hat{\zeta}_2,\ \hat{\zeta}_1,\ \hat{\zeta}_3$ corresponding to the maximum inundation observed for each event. The magnitude of each jump is approximately equal to the probability of the corresponding event, as long as the sum of all probabilities of larger events is much less than 1.

Note that if an additional event were added that gave maximum inundation $\bar{\hat{\zeta}}$ at the (x, y) point being studied, then a new jump discontinuity would be added to the hazard curve at the point $\bar{\hat{\zeta}}$, with the portion of the curve to the left of $\bar{\hat{\zeta}}$ shifted upwards by approximately $\bar{p}$, the probability of occurance of this event. (More exactly by $1 - (1 - \bar{p}) \prod_k (1 - p_k)$ where the product is over all events with inundation $\hat{\zeta}_k > \bar{\hat{\zeta}}$.)

Note also that if there is uncertainty in the exact details of the slip pattern for one of these events, then we might replace the single realization, say AASZe01, by N slightly different realizations, which might give a range of inundations near $\hat{\zeta}_1$. If we assigned each a probability p_1/N, for example, then the hazard curve would be unchanged except in the vicinity of $\hat{\zeta}_1$, where the discontinuity of magnitude $p_{13} - p_3$ would be replaced by N discontinuities each with magnitude roughly $1/N$ as large, distributed near $\hat{\zeta}_1$ at points corresponding to the maximum inundation of each of these N realizations. If we considered a continuous distribution of possible realizations of AASZe01, then this would generally tend to smooth out the discontinuity into a continuous curve between the minimum and maximum inundations observed for different realizations, with the total drop in the exceedance probability over this interval remaining constant at $p_{13} - p_3$. If we do this for each of the events shown in Table 4 and Figure 36, we might get a hazard curve similar to what is shown in Figure 37. As explained in the next section, a similar smoothing of the hazard curve is observed when tidal uncertainty is incorporated, since this also increases the range of inundation values ζ that can be observed for each event.

In practice we do not attempt to compute the hazard curve probabilities for all values of ζ at each (x, y). Instead we choose a finite set of exceedance values ζ_k and determine the probability of exceeding each ζ_k. We then approximate the hazard curve by a piecewise linear function that interpolates these values $(\zeta_k,\ P(\zeta_k; x, y))$. The left plot in Figure 38 shows this approximation for the previous example. We do this because computing each value $P(\zeta_k; x, y)$ requires combining information from all simulation runs together with tidal variation, as described in the next section, and is somewhat costly to perform. By choosing a finite set of ζ_k values the postprocessing is also simplified.

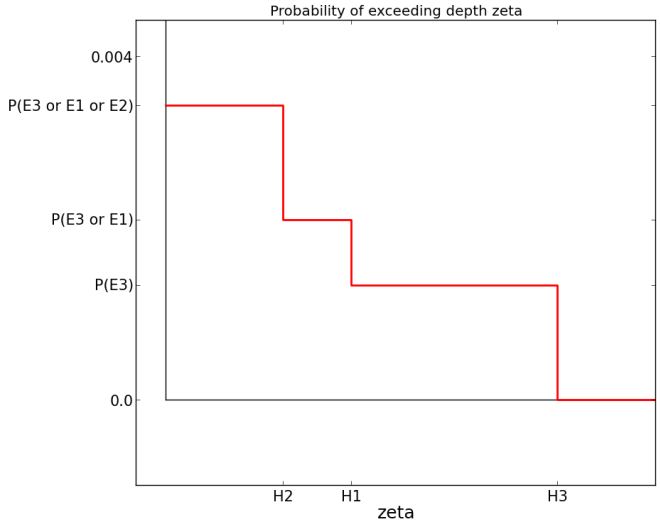

Figure 36: Sample hazard curve for a fixed (x, y) point when three distinct events are considered that give inundation to three depths. Using the data from Table 4.

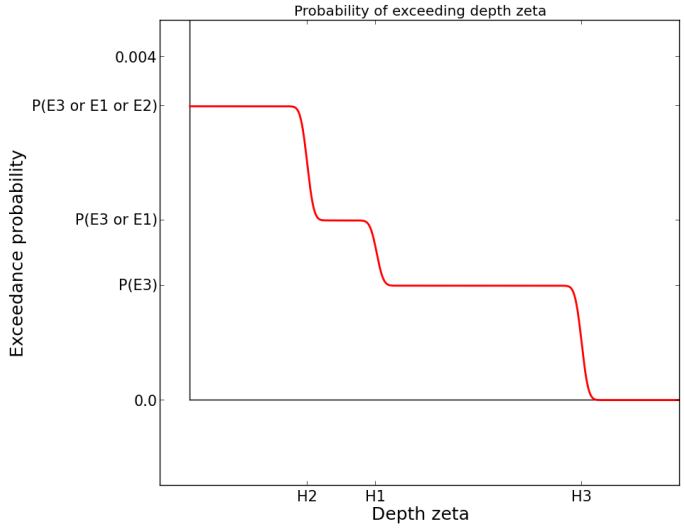

Figure 37: Sample hazard curve as in Figure 36, but with uncertainty in the amplitude added. The probability of each event is the same as before, but the extent of inundation may vary between different realizations, leading to a spreading of the jump discontinuity.

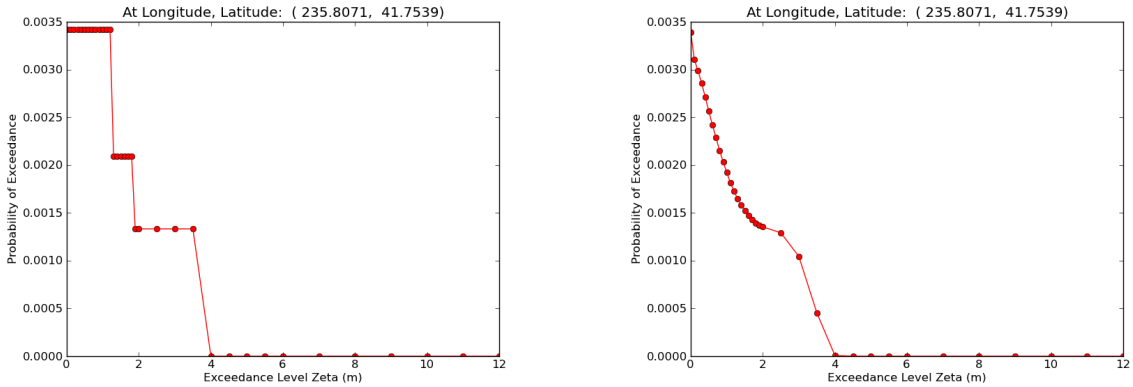

Figure 38: Sample hazard curve for a fixed (x, y) point when three distinct events are considered that give inundation to three depths. Left: Using the data from Table 4, as in Figure 36 but illustrating the use of a finite number of exceedance values ζ_k. Right: Corresponding curve for the same three events but when tidal uncertainty is included.

We have chosen the following exceedance values:

$$\begin{aligned} \zeta_k = 0,\ 0.1,\ 0.2,\ \ldots,\ 1.9,\ 2.0, \\ 2.5,\ 3.0,\ \ldots,\ 5.5,\ 6.0, \\ 7.0,\ ,8.0,\ \ldots,\ 12.0, \end{aligned} \tag{8}$$

which we believe is sufficiently dense to yield good approximations of the hazard curves in general. The curve determined from considering only the three events discussed above is shown in Figure 38.

Once the hazard curve at each (x, y) has been determined, the information contained in this curve can be used in two distinct ways. For a given probability such as $\bar{p} = 0.01$ it is possible to find the corresponding value ζ for which $P(\zeta; x, y) = 0.01$. This could be interpreted as the depth of inundation expected in a "100-year event". By determining this for each (x, y) it is possible to plot the extent of inundation expected with probability $\bar{p}$ and the flow depth at each point inundated.

Conversely, one can choose a particular inundation level $\tilde{\zeta}$ and determine the probability of exceeding this value $P(\tilde{\zeta}; x, y)$ at each point. A contour plot of this value over the spatial (x, y) domain then shows the probability of exceeding $\tilde{\zeta}$ at each point in the community. In particular, choosing $\tilde{\zeta} = 0$ would show probability contours of seeing any flooding. The $p = 0.01$ contour would again correspond to the inundation limit of the "100-year event". This approach and the advantages of generating maps of this form are discussed further in Section 9.2.

B Generating hazard curves including tidal variation

We consider J tsunami events, with event E_j having a recurrence rate ν_j that obeys a Poisson process. That is, the probability that E_j occurs is $P(E_j) = 1 - e^{-\nu_j}$. We are interested in finding the probability that inundation height ζ exceeds level ζ_i at a grid location of interest. Typically, we are interested in all grid locations covering a fixed grid of the Crescent City area.

The probability that E_j does not produce exceedance of ζ_i is

$$1 \; - \; (1 - e^{-\nu_j})\, P(\zeta > \zeta_i \,|\, E_j).$$

Then the probability that at least one event gives exceedance of ζ_i is

$$P(\zeta > \zeta_i) = 1 \; - \; \prod_{j=1}^{J} \left(1 \; - \; (1 - e^{-\nu_j})\, P(\zeta > \zeta_i \,|\, E_j)\right) \; . \tag{9}$$

Furthermore, if event E_j is composed of k_j mutually exclusive realizations, so that when E_j occurs, exactly one of the realizations occurs, say E_{jk}, we can substitute

$$P(\zeta > \zeta_i \,|\, E_j) = \sum_{k=1}^{k_j} P(\zeta > \zeta_i \,|\, E_{jk})\, P(E_{jk} \,|\, E_j)$$

where $\sum_{k=1}^{k_j} P(E_{jk} \,|\, E_j) = 1$ into equation (9) to get

$$P(\zeta > \zeta_i) = 1 \; - \; \prod_{j=1}^{J} \left(1 \; - \; (1 - e^{-\nu_j}) \sum_{k=1}^{k_j} P(\zeta > \zeta_i \,|\, E_{jk})\, P(E_{jk} \,|\, E_j) \right) \; . \tag{10}$$

If we define $\bar{\mu}_{ij}$ as

$$\bar{\mu}_{ij} = (1 - e^{-\nu_j}) \sum_{k=1}^{k_j} P(\zeta > \zeta_i \,|\, E_{jk})\, P(E_{jk} \,|\, E_j), \tag{11}$$

equation (10) can be written as

$$P(\zeta > \zeta_i) = 1 \; - \; \prod_{j=1}^{J} (1 - \bar{\mu}_{ij}) \tag{12}$$

and following the discussion in Section 2.6.1, can be approximated as

$$P(\zeta > \zeta_i) = 1 \; - \; \prod_{j=1}^{J} e^{-\bar{\mu}_{ij}}. \tag{13}$$

If we again use the discussion in Section 2.6.1 to approximate $\bar{\mu}_{ij}$ in equation (11) by μ_{ij}, where

$$\mu_{ij} = \nu_j \sum_{k=1}^{k_j} P(\zeta > \zeta_i \,|\, E_{jk})\, P(E_{jk} \,|\, E_j), \tag{14}$$

we arrive at the expression for $P(\zeta > \zeta_i)$ that was used by González,et.al. [12] in the Seaside, Oregon study. That is,

$$P(\zeta > \zeta_i) = 1 \, - \prod_{j=1}^{J} e^{-\mu_{ij}}. \tag{15}$$

By varying $i = 1 \ldots Z$ to cover more exceedance levels of interest, we can calculate the pairs $(\zeta_i,\ P(\zeta > \zeta_i))$, $i = 1 \ldots Z$ and construct a hazard curve for each fixed grid point of interest.

C The 100- and 500-year Flood: η-contour maps

The *regulatory products* required by FEMA are 100-year and 500-year hazard maps, which are shown in Section 3. These maps show ζ, where ζ was the flow depth on land and the height above MHW for a grid location in the sea. The plots below are the same regulatory products with η plotted, where η is the height above MHW on either the land ($\eta = \zeta + B$) or in the sea ($\eta = \zeta$). For a land point, B is the bathymetry measured above MHW. These four plots are exactly those of Figure 30, with η plotted instead of ζ. For simplicity, and because maximum flow depth ζ is the most easily visualized expression of the physical flooding hazard, we chose to work only with ζ in the body of this report.

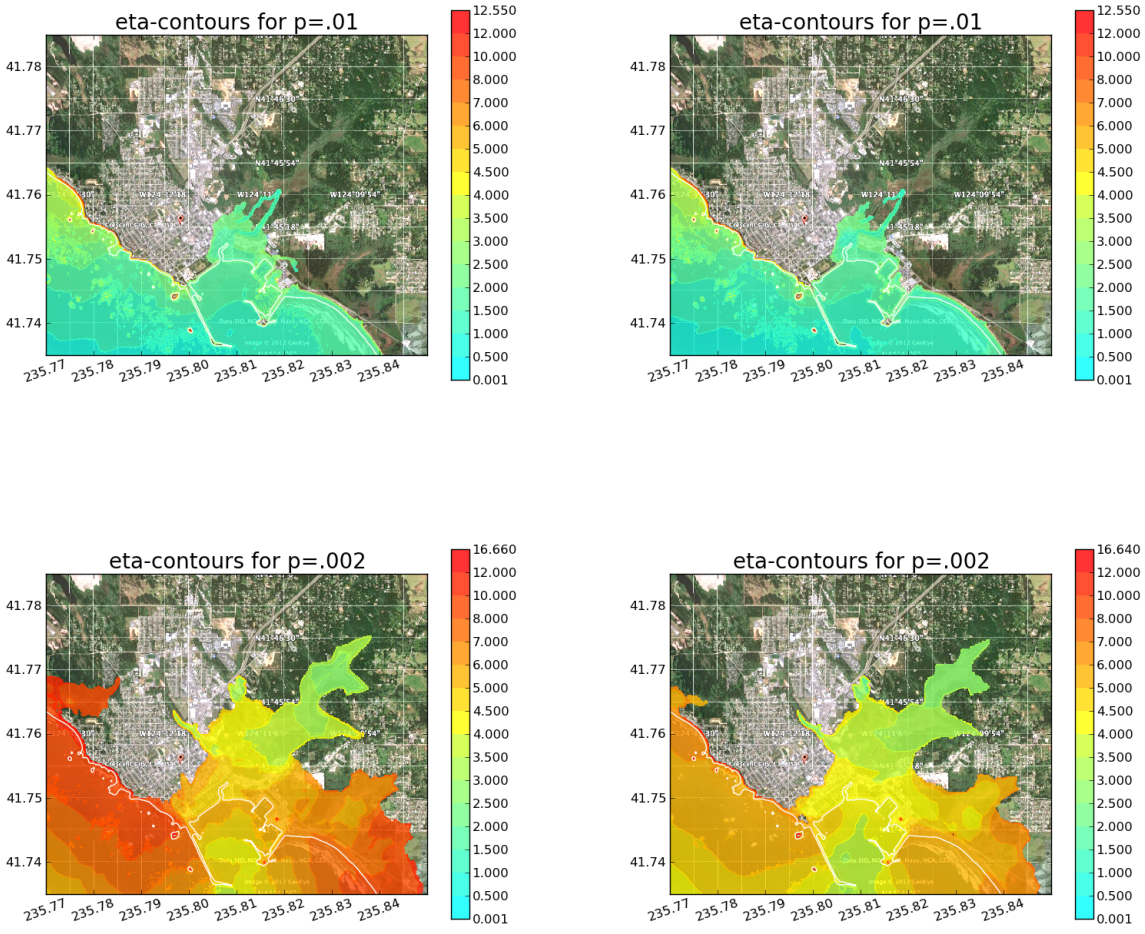

Figure 39: η-contours for Table 1 sources for p=.01 (Top) and p=.002 (Bottom), with $T_M = 332$ (left) and $T_M = 525$ (right)

D Data files

Seven data files will be provided to BakerAECOM to accompany this report, ASCII text format. Each file has 467,965 lines, one for each grid point in the 1/3" grid covering the city and harbor. The files are:

1. `xyB.txt`: The file containing the (x, y) = (longitude, latitude) coordinates of each point in columns 1 and 2 and the topography/bathymetry of the point in column 3. The bathymetry is in meters relative to MHW (positive on land).

2. `Zeta_CSZ332.txt` Column 1 is the ζ value for the 100-year ($p = 0.01$) flood and column 2 is the ζ value for the 500-year ($p = 0.002$) flood. This was computed using all sources in Table 1, assuming a return time of 332 years for the CSZ sources. This is the data plotted in Figure 3 and Figure 4 and in Figure 30.

3. `Zeta_CSZ525.txt` Column 1 is the ζ value for the 100-year ($p = 0.01$) flood and column 2 is the ζ value for the 500-year ($p = 0.002$) flood. This was computed using all sources in Table 1, assuming a return time of 525 years for the CSZ sources. This is the data plotted in Figure 30.

4. `Eta_CSZ332.txt` Column 1 is the η value for the 100-year ($p = 0.01$) flood and column 2 is the η value for the 500-year ($p = 0.002$) flood. This was computed using all sources in Table 1, assuming a return time of 332 years for the CSZ sources. This is the data plotted in Figure 39.

5. `Eta_CSZ525.txt` Column 1 is the η value for the 100-year ($p = 0.01$) flood and column 2 is the η value for the 500-year ($p = 0.002$) flood. This was computed using all sources in Table 1, assuming a return time of 525 years for the CSZ sources. This is the data plotted in Figure 39.

6. `exceedance_probs_CSZ332.txt` This file has 35 columns, giving the probability of exceedance for each of 35 different exceedance levels ζ_i for $i = 1,\ 2,\ \ldots,\ 35$ as listed in (8) and repeated here:

$$\begin{aligned}\zeta_k = 0,\ 0.1,\ 0.2,\ &\ldots,\ 1.9,\ 2.0,\\ 2.5,\ 3.0,\ &\ldots,\ 5.5,\ 6.0,\\ 7.0,\ ,8.0,\ &\ldots,\ 12.0.\end{aligned}$$

   Plotting these ζ_i values against a row of the file will produce the hazard curve at the corresponding grid point. This file contains exceedance probabilities when all sources in Table 1 are used, with a return time of 332 years for CSZ.

7. `exceedance_probs_CSZ525.txt` This file has 35 columns, as described in #6 but using a return time of 525 years for CSZ.